

---

# TENSOR GAUSSIAN PROCESS WITH CONTRACTION FOR MULTI-CHANNEL IMAGING ANALYSIS

---

A PREPRINT

**Hu Sun, Ward Manchester, Meng Jin, Yang Liu, Yang Chen\***

January 27, 2023

## ABSTRACT

Multi-channel imaging data is a prevalent data format in scientific fields such as astronomy and biology. The structured information and the high dimensionality of these 3-D tensor data makes the analysis an intriguing but challenging topic for statisticians and practitioners. The low-rank scalar-on-tensor regression model, in particular, has received widespread attention and has been re-formulated as a tensor Gaussian Process (Tensor-GP) model with multi-linear kernel in [30]. In this paper, we extend the Tensor-GP model by integrating a dimensionality reduction technique, called *tensor contraction*, with a Tensor-GP for a scalar-on-tensor regression task with multi-channel imaging data. This is motivated by the solar flare forecasting problem with high dimensional multi-channel imaging data. We first estimate a latent, reduced-size tensor for each data tensor and then apply a multi-linear Tensor-GP on the latent tensor data for prediction. We introduce an anisotropic total-variation regularization when conducting the tensor contraction to obtain a sparse and smooth latent tensor. We then propose an alternating proximal gradient descent algorithm for estimation. We validate our approach via extensive simulation studies and applying it to the solar flare forecasting problem.

## 1 Introduction

Regression models that deal with scalar labels and tensor covariates, i.e. scalar-on-tensor regression, have received widespread attention over the past decade [9, 32, 31, 12, 17, 19]. Given paired observations  $\{(\mathcal{X}_i, y_i)\}_{i=1}^N$ , where  $\mathcal{X}_i \in \mathbb{R}^{I_1 \times I_2 \times \dots \times I_m}$ , the existing literature approaches the regression problem via:

$$\mathbb{E}[y|\mathcal{X}] = \alpha + \langle \mathcal{W}, \mathcal{X} \rangle \quad (1)$$

where  $\mathcal{W}$  is the regression coefficient tensor that matches the shape of  $\mathcal{X}$  and  $\langle \cdot, \cdot \rangle$  denotes tensor inner product following [14]. This formulation can be readily adopted under the framework of generalized linear model [32] while simultaneously preserving the tensor structure of the covariates  $\mathcal{X}$ . Typically, tensor data is of ultra-high dimensions. Various constraints have been introduced on  $\mathcal{W}$ , such as tensor norm regularization [6, 31] and tensor rank constraints [19, 7]. These constraints induce a sparse and low-rank structure over  $\mathcal{W}$ , making inferences of the high-order correlation between the scalar label and the tensor covariates tractable and interpretable.

Gaussian Process (GP) [29] is an alternative approach to modeling complex correlation structures, and has been applied to a tensor regression problem in [12], where a GP prior is imposed on  $\mathcal{W}$ . In [30], it is established that the tensor regression model (1), together with a low-rank constraint ( $\text{rank}(\mathcal{W}) \leq R$ ), leads to the same estimator  $\widehat{\mathcal{W}}$  as the tensor Gaussian Process (**Tensor-GP**) coupled with a multi-linear kernel on the prior of  $\mathcal{W}$ . A multi-linear kernel function  $k(\cdot, \cdot)$  for  $m$ -mode tensors  $\mathcal{X} \in \mathbb{R}^{I_1 \times I_2 \times \dots \times I_m}$  can be defined in a Kronecker product form:

$$k(\mathcal{X}_i, \mathcal{X}_j) = \text{vec}(\mathcal{X}_i)^\top (\otimes_{m'=1}^m K_{m'}) \text{vec}(\mathcal{X}_j),$$

---

\* All correspondence shall go to Hu Sun, [husun@umich.edu](mailto:husun@umich.edu), Department of Statistics, University of Michigan, Ann Arbor, and Yang Chen, [ychenang@umich.edu](mailto:ychenang@umich.edu), Department of Statistics and the Michigan Institute for Data Science (MIDAS), University of Michigan, Ann Arbor

where  $\text{vec}(\cdot)$  is the vectorization operator and  $\otimes$  denotes the matrix Kronecker product and  $K_1, \dots, K_m$  captures the mode-specific covariance structure of the regression coefficient tensor and are assumed to be low-rank. Interpreting this GP regression model can be hard since one needs to inspect the multi-linear kernel which deals with the tensor data at its original dimensionality  $d = \prod_{m'=1}^m I_{m'}$ .

The capability of the multi-linear Tensor-GP to provide uncertainty quantification on the prediction makes it an attractive alternative to its low-rank tensor regression model counterpart, but a sufficient dimension reduction on the tensor data is required to make it readily interpretable for scientific applications. In [15], a tensor contraction operation is introduced before estimating the tensor regression model. Instead of compressing the information of tensor data into a vector like most deep neural networks (e.g. Variational Auto-encoder [13]), the tensor data is contracted into a smaller “core” tensor with the same number of modes. Such a dimension reduction technique preserves the tensor structure of the data, making tensor regression or Tensor-GP directly applicable.

In this paper, we propose a novel framework combining the merits of tensor contraction and Tensor-GP for the scalar-on-tensor regression task. Our framework consists of two major steps. First, we introduce a tensor contraction step using tensor mode product to reduce the dimensionality of the tensor data  $\mathcal{X}$ . This transforms the original tensor  $\mathcal{X}$  to a much smaller latent tensor  $\mathcal{Z}$ . Second, we adopt the multi-linear Tensor-GP on the reduced-sized tensor  $\mathcal{Z}$  for the regression task. We build our model around a special type of tensor, i.e. the multi-channel imaging dataset, motivated by an application to astrophysical imaging analysis. But our model can be easily extended to a general tensor setup. We summarize our contributions as follows:

- We integrate tensor dimension reduction with Tensor-GP in a unified framework called **Tensor-GPST**, allowing for learning a low-dimensional tensor representation in a supervised learning context.
- We propose to use the anisotropic total variation penalty [28] in the tensor contraction step for a sparse and spatially smooth tensor dimension reduction. We estimate the parameters of Tensor-GPST jointly under a penalized marginal likelihood approach coupled with the proximal gradient method.

## 2 Tensor Gaussian Process with Spatial Transformation (Tensor-GPST)

### 2.1 Method

We consider a multi-channel imaging dataset  $\{(\mathcal{X}_i, y_i)\}_{i=1}^N$ , where  $\mathcal{X}_i \in \mathbb{R}^{H \times W \times C}$ ,  $y_i \in \mathbb{R}$ .  $H, W, C$  are the height, width and number of channels, respectively. Any single channel is denoted as  $\mathcal{X}_i^{(c)} \in \mathbb{R}^{H \times W}$ ,  $c = 1, 2, \dots, C$ . We use  $\mathbf{X} \in \mathbb{R}^{N \times H \times W \times C}$  and  $\mathbf{y} \in \mathbb{R}^N$  to denote the concatenated imaging data and regression labels. Gaussian process regression (GPR) specifies a GP prior for  $y_i$  as:

$$y_i = f(\mathcal{X}_i) + \epsilon_i, \quad f(\cdot) \sim \text{GP}(m(\cdot), k(\cdot, \cdot)) \quad (2)$$

with  $\epsilon_i \sim \mathcal{N}(\mathbf{0}, \sigma^2)$  being the idiosyncratic noise. GP prior characterizes the unknown function  $f(\cdot)$  evaluated at all data points as a joint Gaussian distribution, with a mean function  $m(\cdot)$  and a covariance kernel function  $k(\cdot, \cdot)$ . Typically, the mean function is assumed to be zero and the covariance kernel fully specifies the behavior of the GP prior.

Based on the baseline GP setup, we consider a two-layer model where the first layer condenses the information of any multi-channel imaging data  $\mathcal{X}_i \in \mathbb{R}^{H \times W \times C}$  into a reduced-sized tensor  $\mathcal{Z}_i \in \mathbb{R}^{h \times w \times C}$  via tensor mode product:

$$\mathcal{Z}_i = \mathcal{X}_i \times_1 A \times_2 B \times_3 \mathbf{I}_C \quad (3)$$

with  $A \in \mathbb{R}^{h \times H}$ ,  $B \in \mathbb{R}^{w \times W}$  and  $h < H, w < W$ . Both  $A$  and  $B$  reduce the dimension of individual channel data  $\mathcal{X}_i^{(c)}$  from  $H \times W$  to  $h \times w$  via a bi-linear transformation:

$$\mathcal{Z}_i^{(c)} = A \mathcal{X}_i^{(c)} B^\top, \quad c = 1, 2, \dots, C$$

This formulation for contracting the dimensionality of tensor data can be found in a more general setting in tensor regression networks [15], known as the tensor contraction layer. In our method, we envelope the tensor contraction operation within a tensor Gaussian process regression framework. We further assume that all channels share the same tensor contracting factors  $A$  and  $B$ . This assumption aims at preserving the multi-channel structure of the reduced-sized tensor  $\mathcal{Z}$  for the ease of interpretation.

One can interpret the transformed tensor data  $\mathcal{Z}_i$  as the “latent” low-dimensional representation of the original tensor data  $\mathcal{X}_i$ . Each  $(s, t)$ -th element of  $\mathcal{Z}_i^{(c)}$  is constructed via a matrix inner product with a rank-1 “feature map”:

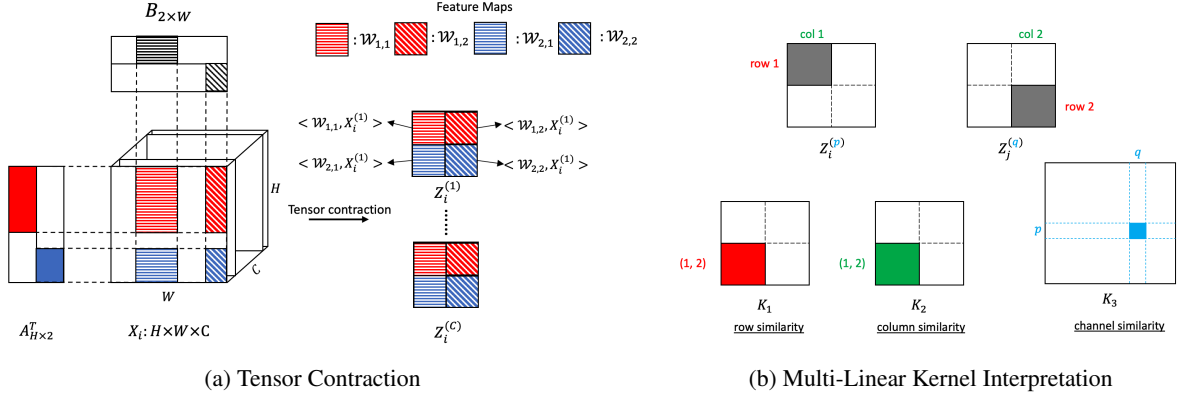


Figure 1: (a) Example of the tensor contraction step for tensor data  $\mathcal{X}_i \in \mathbb{R}^{H \times W \times C}$  to its latent tensor  $\mathcal{Z}_i \in \mathbb{R}^{2 \times 2 \times C}$ . The tensor contracting factors  $A, B$  are sparse (colored/dashed bands indicate nonzero elements) and they jointly extract features from  $\mathcal{X}_i^{(1)}, \dots, \mathcal{X}_i^{(C)}$  with rank-1 feature maps  $\{\mathcal{W}_{1,1}, \mathcal{W}_{1,2}, \mathcal{W}_{2,1}, \mathcal{W}_{2,2}\}$ . Each channel of  $\mathcal{Z}_i^{(c)}$  has  $2 \times 2$  features, based on the inner product of every feature map with the channel data  $\mathcal{X}_i^{(c)}$ . (b) Example of the multi-linear kernel with a pair of latent tensor data  $(\mathcal{Z}_i, \mathcal{Z}_j)$ . Any pair of pixels in  $\mathcal{Z}_i$  and  $\mathcal{Z}_j$ , e.g.  $Z_i^{(p)}(1, 1)$  and  $Z_j^{(q)}(2, 2)$  in the plot (gray), are weighted by the product of their row similarity  $K_1(1, 1)$  (red), column similarity  $K_2(2, 2)$  (green) and channel similarity  $K_3(p, q)$  (blue). See (45) for a formulaic explanation.

$\mathcal{Z}_i^{(c)}(s, t) = \langle \alpha_s^\top \beta_t, \mathcal{X}_i^{(c)} \rangle$ , where  $\alpha_s$  and  $\beta_t$ , the bases of the feature map, are the  $s^{\text{th}}$  and  $t^{\text{th}}$  rows of  $A$  and  $B$  respectively. We denote the feature map  $(\alpha_s^\top \beta_t)$  as  $\mathcal{W}_{s,t} \in \mathbb{R}^{H \times W}$  in the remainder of the paper. A visual explanation of the tensor contraction operation with a toy example ( $h = w = 2$ ) is shown in Figure 1a. Since we preserve the tensor structure in the latent space, any slice of  $\mathcal{Z}_i$  along the first or second mode share the same feature map basis  $\alpha_s$  or  $\beta_t$ .

Given the transformed tensor data  $\mathcal{Z}_i \in \mathbb{R}^{h \times w \times C}$ , we assume a GP prior for  $\mathbf{y} = (y_1, y_2, \dots, y_N)^\top$  given  $\mathcal{Z}_1, \mathcal{Z}_2, \dots, \mathcal{Z}_N$  with a multi-linear kernel following [30]:

$$y_i = g(\mathcal{Z}_i) + \epsilon_i, \quad g(\cdot) \sim \text{GP}(0, k(\cdot, \cdot)), \quad (4)$$

where  $k(\cdot, \cdot)$  is the multi-linear tensor kernel function  $k(\cdot, \cdot)$ :

$$k(\mathcal{Z}_i, \mathcal{Z}_j) = \text{vec}(\mathcal{Z}_i)^\top (K_3 \otimes K_2 \otimes K_1) \text{vec}(\mathcal{Z}_j). \quad (5)$$

In this model,  $K_1 \in \mathbb{R}^{h \times h}$ ,  $K_2 \in \mathbb{R}^{w \times w}$ ,  $K_3 \in \mathbb{R}^{C \times C}$  capture the mode-specific covariance structure and can be assumed as being low-rank.

It has been shown that the multi-linear tensor GP can be interpreted as the probabilistic version of the low-rank tensor regression [30]. Thus the model specified by (4) and (5), together with the tensor contraction in (3), can be rewritten as a tensor regression model with an extra dimension reduction step:

$$\begin{aligned} y_i &= \langle \mathcal{W}, \mathcal{Z}_i \rangle + \epsilon_i \\ &= \langle \mathcal{W}, \mathcal{X}_i \times_1 A \times_2 B \times_3 \mathbf{I}_C \rangle + \epsilon_i \end{aligned} \quad (6)$$

where  $\mathcal{W} \in \mathbb{R}^{h \times w \times C}$  is the regression coefficient tensor with the same shape as the latent tensor  $\mathcal{Z}_i$ . This tensor regression model can be regarded as a two-layer tensor regression network with a tensor contraction layer and a tensor regression layer, as discussed in [15].

Combining (3), (4) and (5) together, and using the property of vectorizing tensor mode product, our method essentially specifies the following tensor GP:

$$y_i = f(\mathcal{X}_i) + \epsilon_i, \quad f(\cdot) \sim \text{GP}(0, \mathcal{K}) \quad (7)$$

$$\mathcal{K}(\mathcal{X}_i, \mathcal{X}_j) = \text{vec}(\mathcal{X}_i)^\top (K_3 \otimes K_2^* \otimes K_1^*) \text{vec}(\mathcal{X}_j) \quad (8)$$

$$K_2^* = B^\top K_2 B, \quad K_1^* = A^\top K_1 A \quad (9)$$

and we name the framework **Tensor Gaussian Process with Spatial Transformation** (Tensor-GPST), where  $A$  and  $B$  transforms, in a bi-linear way, the spatial information contained in the imaging data.

An equivalent way of expressing the model is via tensor regression on the original tensor  $\mathcal{X}$ . Given the formulation in (1), we essentially assume a Gaussian prior over  $\mathcal{W}$ :

$$\begin{aligned}\text{vec}(\mathcal{W}) &\sim (\mathbf{I}_C \otimes B \otimes A)^\top \text{vec}(\mathcal{T}), \mathcal{T} \in \mathbb{R}^{h \times w \times C} \\ \text{vec}(\mathcal{T}) &\sim \mathcal{N}(\mathbf{0}, K_3 \otimes K_2 \otimes K_1)\end{aligned}\quad (10)$$

which is similar to a tensor factor model [3, 8] coupled with a Gaussian factor with Kronecker-product covariance structure.

## 2.2 Estimating Algorithm

To estimate the model parameters of Tensor-GPST in (7)-(9), i.e. the tensor contracting factors  $(A, B)$ , the multi-linear kernel factors  $(K_1, K_2, K_3)$ , and the idiosyncratic noise variance  $\sigma^2$ , we follow the general GP estimation technique and minimize the negative marginal Gaussian log-likelihood  $\ell(\mathbf{y}|A, B, K_1, K_2, K_3, \sigma)$ :

$$\ell = \frac{1}{2} \log |\mathbf{K} + \mathbf{D}_\sigma| + \frac{1}{2} \mathbf{y}^\top (\mathbf{K} + \mathbf{D}_\sigma)^{-1} \mathbf{y} + \text{const} \quad (11)$$

where  $\mathbf{K}$  is an  $N \times N$  empirical kernel matrix computed via the kernel function (8) for all pairs of tensor data.

To speed up the computation, we approximate each multi-linear kernel factor with a factorized form:

$$K_1 = U_1^\top U_1, K_2 = U_2^\top U_2, K_3 = U_3^\top U_3 \quad (12)$$

where  $U_1 \in \mathbb{R}^{r_1 \times h}, U_2 \in \mathbb{R}^{r_2 \times w}, U_3 \in \mathbb{R}^{r_3 \times C}$ .  $U_1, U_2, U_3$  are orthogonal matrices with  $r_1 \leq h, r_2 \leq w, r_3 \leq C$ . The tuning parameter is set as such that  $r_1 = h, r_2 = w, r_3 = C$  throughout the paper but can be set to smaller values to speed up the computation. With the factorization assumption, one can decompose the empirical kernel matrix  $\mathbf{K}$  as:  $\mathbf{K} = \tilde{\mathbf{U}} \tilde{\mathbf{U}}^\top$ , where:

$$\tilde{\mathbf{U}} = \mathcal{X}^\top (\mathbf{I}_C \otimes B \otimes A)^\top (U_3 \otimes U_2 \otimes U_1)^\top$$

where  $\mathcal{X} = [\text{vec}(\mathcal{X}_1); \text{vec}(\mathcal{X}_2); \dots; \text{vec}(\mathcal{X}_N)]$ . The factorized form of  $\mathbf{K}$  can simplify the computation of the gradients since one can invert the covariance matrix  $(\mathbf{K} + \mathbf{D}_\sigma)$  with the Woodbury identity, as done in [30].

Since the tensor contracting factors  $(A, B)$  are extracting spatial features from each channel of the image, we assume that each spatial feature can be constructed from several spatially-contiguous regions, and this leads us to the assumption that each feature map  $\mathcal{W}_{s,t} = \alpha_s^\top \beta_t$  has some degrees of spatial smoothness. We introduce the spatial smoothness assumption into our model via penalizing the anisotropic total variation norm  $\|\mathcal{W}_{s,t}\|_{\text{TV}}$ :

$$\begin{aligned}\|\mathcal{W}_{s,t}\|_{\text{TV}} &= \sum_{i=1}^{H-1} \sum_{j=1}^W |\mathcal{W}_{s,t}(i+1, j) - \mathcal{W}_{s,t}(i, j)| \\ &\quad + \sum_{i=1}^H \sum_{j=1}^{W-1} |\mathcal{W}_{s,t}(i, j+1) - \mathcal{W}_{s,t}(i, j)|.\end{aligned}$$

A more general class of total variation norm penalty on tensor regression model coefficients can be found in [28].

In Lemma 2.1, we derive a simplified form of  $\|\mathcal{W}_{s,t}\|_{\text{TV}}$ , making the estimation of  $A$  and  $B$  a much easier task.

**Lemma 2.1.** *The anisotropic total variation (TV) norm on feature map  $\{\mathcal{W}_{s,t}\}_{s,t=1}^{h,w}$  induces a fused-lasso [25] penalization on  $A$  (and  $B$ ):*

$$\sum_{s=1}^h \sum_{t=1}^w \|\mathcal{W}_{s,t}\|_{\text{TV}} = \|\nabla_x B\|_1 \|A\|_1 + \|B\|_1 \|\nabla_x A\|_1 \quad (13)$$

where  $\nabla_x$  computes the horizontal gradient of a matrix, i.e.  $\nabla_x A_{m \times n}(i, j) = \mathbf{I}_{\{j=n\}} [A(i, j+1) - A(i, j)]$ . We denote the penalty as  $R(A, B)$  throughout the remainder of the paper.

The proof is straightforward by plugging in the formula of each feature map  $\mathcal{W}_{s,t}$ . We leave the details to Appendix A.

The fused-lasso penalty penalizes the sparsity and smoothness of  $A$ , weighted by the smoothness and sparsity of  $B$  and vice versa. Jointly, our estimating problem is attempting to minimize the following penalized negative log-likelihood  $L$ :

$$L(A, B, U_{1:3}, \sigma) := \ell(A, B, U_{1:3}, \sigma) + \lambda R(A, B) \quad (14)$$

The total variation penalty can create feature maps with sharp edges and leads to sparsity for interpretation. In the estimating algorithm, we use proximal gradient descent to estimate the tensor contracting factors ( $A, B$ ) and cyclically update the parameters in the order of:  $A \rightarrow B \rightarrow (U_1, U_2, U_3) \rightarrow \sigma \rightarrow A \rightarrow \dots$ . The fused-lasso penalty over  $A$  and  $B$  makes the proximal step a well-defined *fused lasso 1-D signal approximation* problem [5]. Specifically, at the  $k$ -th iteration, we first propose a gradient descent update for  $A$ , namely  $\widehat{A}^{(k+\frac{1}{2})}$ . Then the final updated value for  $A$ , i.e.  $\widehat{A}^{(k+1)}$ , is the minimizer of the proximal step:

$$\begin{aligned}\widehat{A}^{(k+1)} &= \text{prox}_{\text{TV}}\left(\widehat{A}^{(k+\frac{1}{2})}\right) \\ &= \arg \min _A\left\{\frac{1}{2 \eta_k}\left\|A-\widehat{A}^{(k+\frac{1}{2})}\right\|^2+\lambda R(A, \widehat{B}^{(k)})\right\}\end{aligned}$$

which can be easily solved by first solving the minimization without the  $\ell_1$ -penalty on  $A$  and then apply a soft-thresholding operator to obtain the exact minimizer (see Proposition 1 of [5] for the justification). The same procedure applies when one updates  $B$ .

We summarize the outline of the estimating algorithm in Algorithm 1 and provide the details of the derivation of gradients and the proximal step in Appendix B.

---

**Algorithm 1** Alternating Proximal Gradient Descent Algorithm for Tensor-GPST

---

```

1: Initialize  $\widehat{A}^{(0)}, \widehat{B}^{(0)}, \widehat{U}_1^{(0)}, \widehat{U}_2^{(0)}, \widehat{U}_3^{(0)}, \widehat{\sigma}^{(0)}$  randomly.
2:  $i \leftarrow 0$ 
3: while not converge and  $i \leq \text{max-iter}$  do
4:    $\widehat{A}^{(i+\frac{1}{2})} \leftarrow \widehat{A}^{(i)} - \eta_i \frac{\partial \ell}{\partial A}(\widehat{A}^{(i)}, \widehat{B}^{(i)}, \widehat{U}_{1:3}^{(i)}, \widehat{\sigma}^{(i)})$ 
5:    $\widehat{A}^{(i+1)} \leftarrow \text{prox}_{\text{TV}}(\widehat{A}^{(i+\frac{1}{2})})$  // Fused-Lasso
6:    $\widehat{B}^{(i+\frac{1}{2})} \leftarrow \widehat{B}^{(i)} - \eta_i \frac{\partial \ell}{\partial B}(\widehat{A}^{(i+1)}, \widehat{B}^{(i)}, \widehat{U}_{1:3}^{(i)}, \widehat{\sigma}^{(i)})$ 
7:    $\widehat{B}^{(i+1)} \leftarrow \text{prox}_{\text{TV}}(\widehat{B}^{(i+\frac{1}{2})})$  // Fused-Lasso
8:   Re-scale  $(\widehat{A}^{(i)}, \widehat{B}^{(i)})$  s.t.  $\|\widehat{A}^{(i)}\|_F = 1$ .
9:   for  $j=1:3$  do
10:     $\widehat{U}_j^{(i+1)} \leftarrow \widehat{U}_j^{(i)} - \eta_i \frac{\partial \ell}{\partial U_j}(\widehat{A}^{(i+1)}, \widehat{B}^{(i+1)}, \widehat{U}_{-j}^{(i)}, \widehat{\sigma}^{(i)})$ 
11:   end for
12:    $\widehat{\sigma}^{(i+1)} \leftarrow \widehat{\sigma}^{(i)} - \eta_i \frac{\partial \ell}{\partial \sigma}(\widehat{A}^{(i+1)}, \widehat{B}^{(i+1)}, \widehat{U}_j^{(i+1)}, \widehat{\sigma}^{(i)})$ 
13:    $i \leftarrow i + 1$ 
14: end while
15: Output:  $\widehat{A}^{(i)}, \widehat{B}^{(i)}, \widehat{U}_{1:3}^{(i)}, \widehat{\sigma}^{(i)}$ 

```

---

Since any pair of  $(A, B)$  can be re-scaled by a constant  $c$  such that:  $(B \otimes A) = (c^{-1}B) \otimes (cA)$ , we re-scale the norm of  $(\widehat{A}^{(k)}, \widehat{B}^{(k)})$  after each iteration to ensure there is no identifiability issue up to a scaling factor for the tensor contraction step. We do not enforce the orthonormality of  $U_1, U_2, U_3$ , but a good initialization can still obtain reasonable approximations [30]. To give a warm-start of the model parameters, one can consider solving a tensor regression problem and a tucker decomposition problem subsequently, as inspired by (6) and (10):

$$\begin{aligned}(\widehat{\mathcal{W}}, \widehat{A}^{(0)}, \widehat{B}^{(0)}) &= \arg \min _{\mathcal{W}, A, B}\left\|y_i-\left\langle\mathcal{X}_i, \mathcal{W} \times_1 A^{\top} \times B^{\top}\right\rangle\right\|^2, \\ \widehat{U}_{1:3}^{(0)} &= \arg \min _{S, U_1, U_2, U_3}\left\|\widehat{\mathcal{W}}-\mathcal{S} \times_1 U_1^{\top} \times_2 U_2^{\top} \times_3 U_3^{\top}\right\|^2.\end{aligned}$$

### 2.3 Theoretical Analysis

In this subsection, we provide the convergence analysis of Algorithm 1. Theorem 2.2 provides the upper bound of the optimized loss function (14) with respect to its global minimum. We show that the total variation penalty and the alternating proximal descent introduce extra gaps between the optimized loss and its global minimum.

**Theorem 2.2.** *Given the loss function in (14), assume that the negative log-likelihood  $\ell(.)$  is convex for any of the four parameter blocks:  $\{A\}, \{B\}, \{U_{1:3}\}, \{\sigma\}$ , conditioning on the remaining three blocks being fixed, and the gradients of  $\ell(.)$  are Lipschitz continuous with Lipschitz constant:  $M_A, M_B, M_U, M_\sigma$ , respectively. Then with a constant learning*

rate  $\alpha \in (0, 1/\max\{M_A, M_B, M_U, M_\sigma\}]$ , the block proximal gradient descent algorithm in Algorithm 1 leads to the following bound on the loss function:

$$4(K+1) \left[ L(\widehat{\theta}^{(K+1)}) - L(\theta^*) \right] \leq \frac{\delta^{(0)}}{2\alpha} \quad (15)$$

$$+ \sum_{k=0}^K h_\lambda(\widehat{A}^{(k+1)} - A^*, \widehat{B}^{(k+1)} - B^*, \widehat{B}^{(k)} - B^*) \quad (16)$$

$$+ \frac{1}{2\alpha} \sum_{k=0}^K \tau(\widehat{\theta}^{(k+1)}, \widehat{\theta}^{(k)}, \theta^*) \quad (17)$$

where  $\widehat{\theta}^{(k)} := (\widehat{A}^{(k)}, \widehat{B}^{(k)}, \widehat{U}_{1:3}^{(k)}, \widehat{\sigma}^{(k)})$  and  $\theta^*$  is the global minimizer of loss (14).  $\delta^{(0)}$  is the squared  $\ell_2$  initialization error,  $h_\lambda(\cdot) \geq 0$  is the total-variation gap (TV-gap) and  $\tau(\cdot) \geq 0$  is the alternating descent gap (ALT-gap).  $K$  is the total number of iterations. As a consequence, if one has any three blocks of parameters fixed at their global minima, the remaining block will converge to the global minima at the rate of  $\mathcal{O}(1/K)$ , which echoes the convergence rate of (proximal) gradient descent.

We leave the proof to Appendix C and make a few remarks.

*Remark 2.3.* As  $\widehat{A}^{(k)} \rightarrow A^*$ ,  $\widehat{B}^{(k)} \rightarrow B^*$ , one has  $h_\lambda(\cdot) \rightarrow 0$ . The TV-gap is incurred because we alternatively update  $A$  and  $B$ , and using the current iteration's estimate of  $A$  (or  $B$ ) for updating  $B$  (or  $A$ ) with the total variation penalty leads to extra errors. See the definition of  $h_\lambda(\cdot)$  in (42).

*Remark 2.4.* As  $\widehat{\theta}^{(k)} \rightarrow \theta^*$ ,  $\tau(\cdot) \rightarrow 0$ . The ALT-gap  $\tau(\cdot)$  arises because we use the current iteration's estimate for all but one block of parameters to estimate the gradient of the remaining block of parameter. If the algorithm terminates at a local minimum, the non-vanishing TV-gap and ALT-gap leads to a non-zero gap for the optimized loss function from the global minimum. See the definition of  $\tau(\cdot)$  in (43).

*Remark 2.5.* Tensor regression models with Tucker-type low-rankness have non-convex negative-likelihood function  $\ell(\cdot)$  [17]. But conditioning on all but one block of parameter,  $\ell(\cdot)$  is convex for each individual block. We do not verify the convexity of  $\ell(\cdot)$  in our particular model due to the complexity of the kernel function. Empirically, as we show in Appendix C and also in [30], such alternating gradient descent algorithm works well with the optimization problem and the loss function decays at the rate of  $\mathcal{O}(1/K)$ .

### 3 Experiments

In this section, we validate our method via both simulation study and applications to an astrophysics dataset for solar flare forecasting. We also compare our method against other benchmark tensor regression models. In particular, we are interested in applications to imaging data where the predictive patterns appear in different channels and various locations within a channel. Such patterns are common in scientific datasets where it is hard to define a “canonical” position of the tensor grid, and different samples with similar scalar labels can have similar patterns up to a shift in location and a change in channel.

#### 3.1 Simulation Study

We simulate a tensor dataset  $\{\mathcal{X}_i\}_{i=1}^N$  with 3 channels and each channel is of size  $25 \times 25$ . For each  $25 \times 25 \times 3$  tensor data  $\mathcal{X}_i$ , we randomly pick one of the three channels as the *signal* channel, with equal probability, and the remaining two channels as the *noise* channels. The noise channel contains i.i.d. pixels from  $\mathcal{N}(0, 0.3)$ , and the signal channel uses the same background noise distribution except a  $5 \times 5$  *signal* block that contains i.i.d. pixels from  $\mathcal{N}(4, 0.3)$ . The location of the  $5 \times 5$  block is fixed at the center of the  $25 \times 25$  image if channel 2 is the signal channel (see Type 2 in Figure 2), and is randomly picked at one of the four corners (top-left, top-right, bottom-left, bottom-right) if channel 1 or 3 is the signal channel (see Type 1 and 3 in Figure 2).

We simulate the tensor contracting factors  $A, B$  with a banded structure, such that  $A$  and  $B$  are extracting features from the  $5 \times 5$  blocks with *signal*, see the bottom of Figure 2 for the example of the contracted tensor. The multi-linear kernel setup and the generating process of the regression labels  $\{y_i\}_{i=1}^N$  are detailed in Appendix D. Generally, channel 2 is simulated such that it is negatively correlated with channel 1 & 3, and channel 1 & 3 are nearly perfectly correlated. As a result, Type 1 & 3 have similar regression labels and differ from those of Type 2.

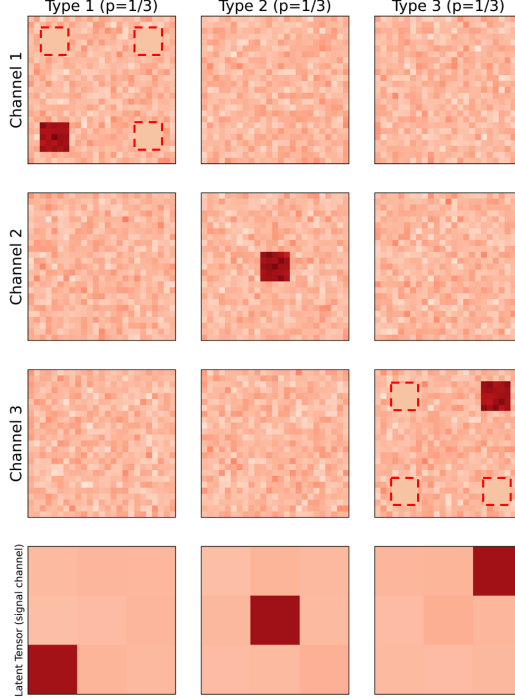


Figure 2: Three types of the simulated tensor data ( $\mathcal{X}_i \in \mathbb{R}^{25 \times 25 \times 3}$ ). Each column is a type (Type 1,2,3) and each consists of one-third of the simulated samples. Each row (row 1-3) is a data channel (channel 1,2,3). Type 1, 2 and 3 have their *signal* channel in channel 1, 2 and 3, respectively. But the location of the  $5 \times 5$  signal block is positioned differently. Type 2 has the signal fixed at the center, while type 1 and 3 has the signal placed, with equal probability, in one of the four corners (dashed block shows the other three possible locations). Samples shown are one realization of the simulation. The latent tensor’s signal channel is shown at the bottom, where during the simulation we set the tensor contraction as a local averaging operator. See details in Appendix D.

With the simulation pattern, we compare our model against these baseline tensor regression models: Tensor-GP (**GP**) [30],  $\ell_2$ -regularized tensor regression with CANDECOMP/PARAFAC (**CP**) tensor rank constraints [6] (**CP**),  $\ell_2$ -regularized tensor regression with Tucker tensor rank constraints [17] (**Tucker**). The tuning parameters are determined by cross-validation. We consider three variations of our model: model with hard constraints on the sparsity of  $(A, B)$  based on the ground truth knowledge (**GPST-Hard**), model with low ( $\lambda = 0.1$ ) total variation penalty (**GPST-low**), and model with high ( $\lambda = 1.0$ ) total variation penalty (**GPST-high**). We simulate the data with size  $N \in \{200, 500\}$  and use 75% for training and 25% for testing and compare the rooted-mean-squared-error (RMSE) on both training and testing across all models above. We set the latent tensor dimension as  $3 \times 3 \times 3$  for **Tensor-GPST** and the rank for  $K_1, K_2, K_3$  of **Tensor-GP** as 3 and the rank as 9 for **CP** and the rank as  $3 \times 3 \times 3$  for **Tucker** such that the low-rankness is comparable across all methods. The simulation experiment is iterated 10 times and the training/testing RMSE is shown in Figure 3.

The Tensor-GP (**GP**) has the worst performance on the testing data and among all Tensor-GPST variants, **GPST-high** achieves comparable regression performance with the tensor regression framework such as **CP** and **Tucker**, and is slightly better than the **GPST-Hard** and **GPST-low**, suggesting that the total variation penalty could help on generalization on testing data. In Table 1, we further include the coverage probability of the 95% confidence intervals on the testing data for the four Gaussian Process regression models. The best performing model is **GPST-Hard**, where we add the exact sparsity on the tensor contracting factors  $A, B$ , and without this knowledge, the **GPST-high** and **GPST-low** perform similarly as compared to **GP**, which indicates that the total variation penalty, though cannot recover the exact sparsity of the underlying truth like **GPST-Hard**, can preserve the uncertainty quantification capability of the Tensor-GP model, and improve the regression performance.

The estimates of the multi-linear kernel and the feature maps by **GPST-high** are visualized in Figure 4. One can see that the feature map  $\mathcal{W}_{2,2}$  and  $\mathcal{W}_{3,2}$  capture the corner and center blocks, and the covariances between the two feature maps are also high, as suggested by  $\widehat{K}_1(2, 3) = 0.77$  and  $\widehat{K}_2(2, 2) = 1.72$ . Channel 1 & 3 have high covariances

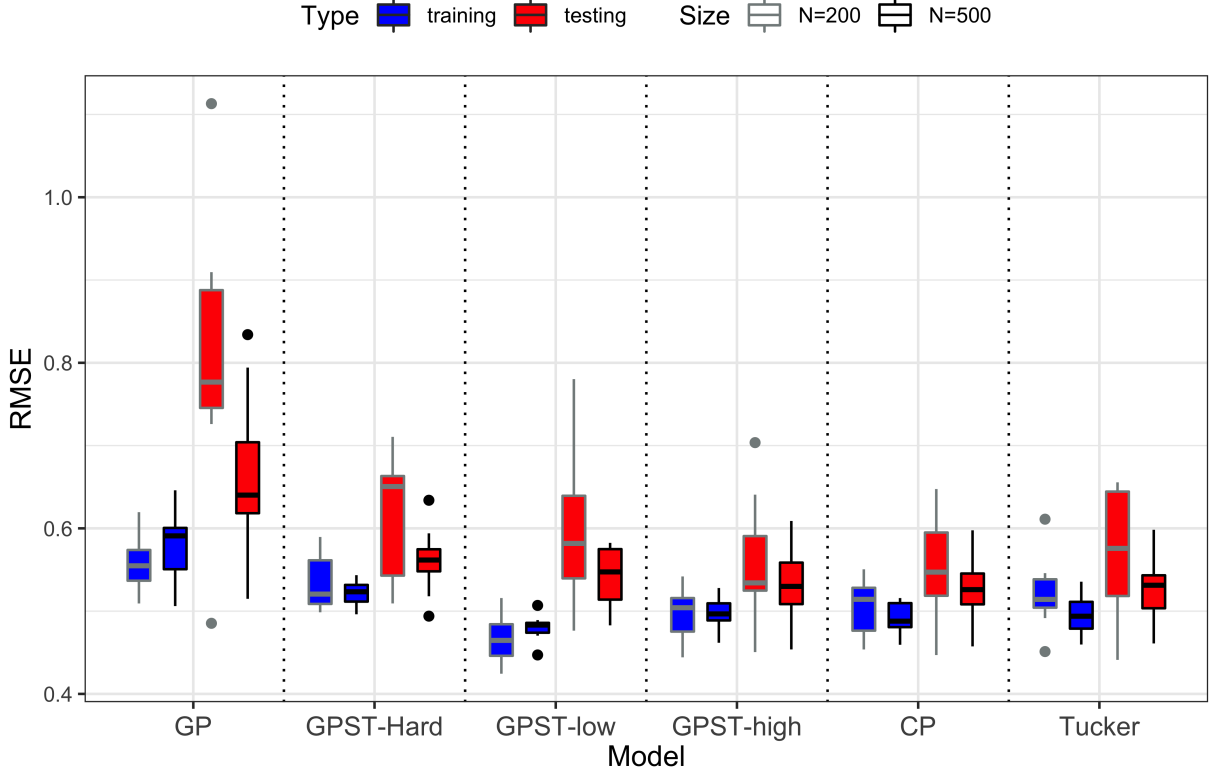


Figure 3: Box plot for the simulation experiment training/testing RMSE of Tensor-GP (**GP**), three variants of Tensor-GPST (**GPST-Hard**, **GPST-low**, **GPST-high**) and tensor regression with CP (**CP**) and Tucker (**Tucker**) low-rankness. The idiosyncratic noise of the data generating model is  $\sigma = 0.5$ , and the result is based on 10 parallel simulation runs.

Model	$N = 200$	$N = 500$
<b>GP</b>	$0.908 \pm 0.058$	$0.952 \pm 0.046$
<b>GPST-Hard</b>	$0.950 \pm 0.046$	$0.975 \pm 0.015$
<b>GPST-low</b>	$0.920 \pm 0.063$	$0.925 \pm 0.038$
<b>GPST-high</b>	$0.930 \pm 0.034$	$0.940 \pm 0.024$

Table 1: Testing Set Coverage Probability of Tensor-GP and Tensor-GPST on 10 parallel simulation runs with  $N \in \{200, 500\}$ . Standard deviation after  $\pm$ .

( $\widehat{K}_3(1, 3) = 3.5$ ), indicating that they share similar ‘‘corner signal’’ patterns and coincides with our ground truth setup (see Figure 7a for the ground truth of  $K_3$ ).

Overall, the simulation experiments convey two main messages:

- Adding the tensor contraction step leads to better regression performances when the signals have low rank structures, and the performance are similar to other low-rank tensor regression frameworks such as **CP** and **Tucker**.
- The anisotropic total variation penalty, though may not fully recover the underlying sparsity of the tensor contracting factors, can improve the regression performance of Tensor-GPST and also provides more direct interpretations.

The inferior performance of Tensor-GP (**GP**), however, is not suggesting that it is an inferior version of GP when dealing with tensor data. The simulation pattern in Figure 2 contains randomness of the signal, making it more beneficial to extract features first using feature maps that cover multiple areas. Directly modeling the covariance structures among all pixels can be difficult in such scenarios.

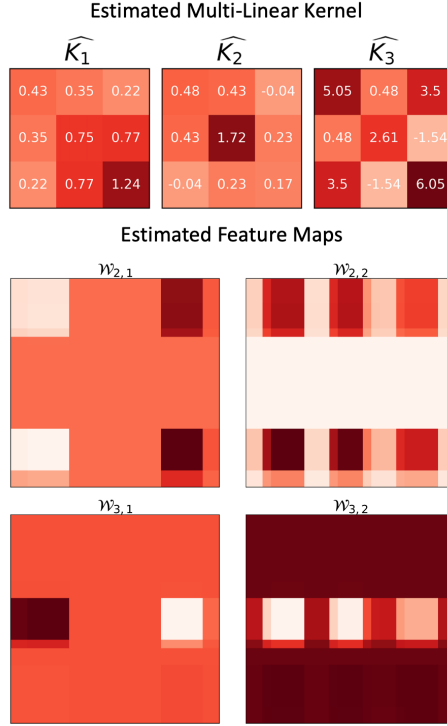


Figure 4: Estimated kernels (top) and non-zero feature maps (bottom) by **GPST-high**.

### 3.2 Application to Solar Flare Forecasting

A solar flare is an intense localized eruption of electromagnetic radiation in the Sun’s atmosphere. Solar flares with high-energy radiation emission can strongly impact the Earth’s space weather and potentially interfere the radio communication of the Earth. Recent works on solar flare forecasting [2, 4, 27, 10, 24] have demonstrated the effectiveness of using machine learning algorithms for forecasting flares, using multivariate time-series physics parameters data or the imaging data known as the Solar Dynamics Observatory (SDO)/Helioseismic and Magnetic Imager (HMI) [21] and SDO/Atmospheric Imaging Assembly (AIA) [16] data. It is shown that these imaging data contain low-dimensional representations that contain flare discriminating signals [23]. Our methodology makes the astrophysical interpretation more accessible as compared to the previous deep neural network approaches.

We consider the specific problem of forecasting the intensity of a solar flare. In our dataset, we have 1,329 flare samples from year 2010 to 2018, consisting of a total of 479 M-class and X-class flares and 850 B-class flares. The class of a flare is determined by the X-ray brightness at its peak, and B-class flare has its brightness within  $10^{-7} \sim 10^{-6}$  W/m<sup>2</sup>, which is considered weak and barely harmful, while the minimum M-class and X-class flares have brightness above  $10^{-5}$  and  $10^{-4}$  W/m<sup>2</sup> respectively. These more energetic flares are capable of heating and ionizing the upper atmosphere resulting in brief radio blackouts and increased satellite drag. We collect the AIA-HMI imaging data for each flare, 1 hour prior to its peak, and each flare data is a 10-channel tensor data of size  $50 \times 50 \times 10$ . We leave the data preprocessing steps and the astrophysical background to Appendix E.

Our goal here is to utilize the 10-channel tensor data ( $\mathcal{X}_i$ ) to predict the flare intensity ( $y_i$ ) and find the discriminating factors for M/X-class and B-class flares. We randomly split our dataset into a 70% training set (340 M/X/591 B) and a 30% testing set (139 M/X/259 B), and log-transforms the flare intensity such that the B-class flare has  $y_i \leq -0.5$  and M/X-class flare has  $y_i \geq 0.5$ .

Similar to the simulation study, we report the solar flare intensity prediction result across five different models: Tensor-GP (**GP**), Tensor-GPST with  $\lambda = 0.1$  (**GPST-low**), Tensor-GPST with  $\lambda = 1.0$  (**GPST-high**), tensor regression with CP rank constraints (**CP**) and tensor regression with Tucker rank constraints (**Tucker**). The hyperparameters are set such that the models have the same latent dimensionality ( $3 \times 3 \times 3$ ) or the rank (9 for **CP** and  $3 \times 3 \times 3$  for **Tucker**) of the regression coefficients. The metrics used are mean-squared error (MSE), R-squared and coverage probability. Additionally, we consider transforming the regression model to a binary classification model by thresholding the

prediction at 0.0 such that any  $\hat{y}_i \geq 0$  indicates an M/X-class flare and any  $\hat{y}_i < 0$  indicates a B-class flare. Then we evaluate the resulting binary classification model with True Skill Statistics (TSS)<sup>2</sup>. A skillful binary classifier for weak vs. strong solar flare is desirable for operational use. Results on the training and testing set are summarized in Table 2, with training set results at the top for each model. Besides random train/test splitting, we also consider chronological split where we group all 931 flares peaked on or before Nov 2nd, 2013 as the training set and the remaining flares as testing. The results for chronological split are summarized in Table 3 in Appendix F.

Model	MSE	R <sup>2</sup>	Pcover	TSS
<b>GP</b>	<b>0.409</b>	<b>0.357</b>	0.963	<b>0.487</b>
	0.569	0.159	0.920	0.364
<b>GPST-low</b>	0.439	0.310	<b>0.966</b>	0.451
	0.462	0.260	0.957	0.441
<b>GPST-high</b>	0.432	0.319	0.959	0.452
	<b>0.432</b>	<b>0.301</b>	<b>0.962</b>	<b>0.446</b>
<b>CP</b>	0.471	0.260	—	0.408
	0.457	0.266	—	0.431
<b>Tucker</b>	0.470	0.261	—	0.408
	0.456	0.266	—	0.431

Table 2: Solar Flare intensity regression results on training (top) and testing (bottom) set across five different models under random train/test splitting. The metrics are mean-squared-error (MSE), R-squared, Coverage Probability (Pcover), True Skill Statistics (TSS). **GPST-high** achieves better testing set performance across all categories. The estimated  $\hat{\sigma}$  for **GP**, **GPST-low**, **GPST-high** are 0.667, 0.668 and 0.662, respectively.

Tensor-GP (**GP**) shows worse generalizability on the testing data. Similar to the simulated data, the flare data exhibits randomness of the location of flare predictive signals. The other four methods show less overfitting and **GPST-high** yields slightly better performances compared to the other methods. In Figure 5, we visualize the feature map with the highest % of explained variation (see definition in (46)). The feature map captures the discriminating signals around the border, indicating that the learnt feature is collected around the perimeter of the flare eruptive region, which is confirmed by the class-average AIA-131Å shown in Figure 5. The complete results are included in Appendix F.

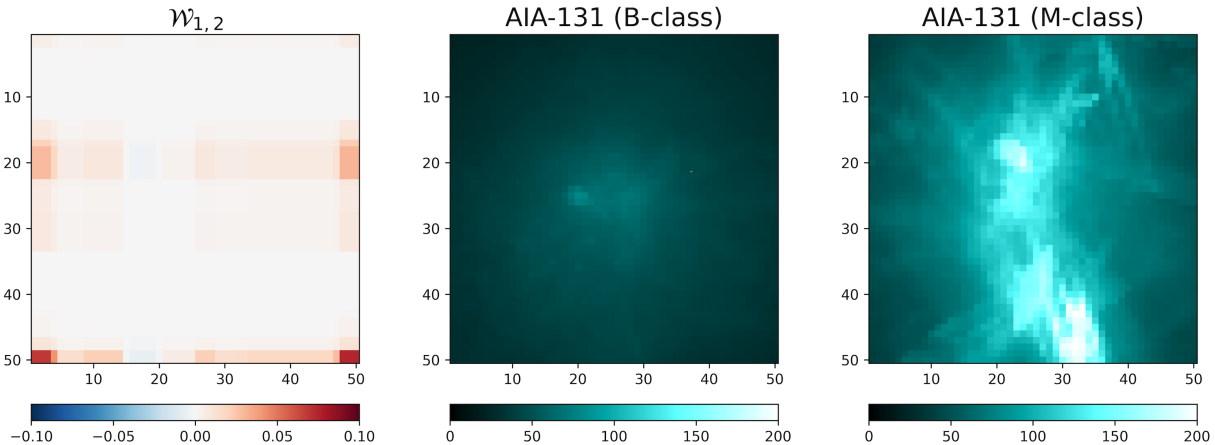


Figure 5: Solar Flare intensity regression results. (a) The most significant feature map  $\mathcal{W}_{1,2}$ . (b) The average AIA-131Å for all B-class flares. (c) The average AIA-131Å for all M/X-class flares.

## 4 Conclusion

In this paper, we construct a new methodology called **Tensor-GPST** for fitting Gaussian Process Regression (GPR) model on multi-channel imaging data. We propose a tensor contraction operation to reduce the dimensionality of the tensor and also introduce anisotropic total variation penalty to the tensor contraction parameters to allow for interpretable

<sup>2</sup>True Skill Statistics is defined as: TSS = TP/(TP+FN) – FP/(FP+TN), where TP, TN, FP, FN represents true positive, true negative, false positive and false negative in the confusion matrix.

feature extraction. We see improvements on the regression performances over the original Tensor-GP [30] in both simulation and solar flare forecasting tasks. The capability of the model in generating an interpretable low-dimensional tensor representation makes it an ideal alternative to the existing tensor regression models in scientific applications.

The current model has several limitations that can potentially lead to future research directions. First, we do not impose explicit identifiability constraints between the tensor contraction parameters and the multi-linear kernel parameters. This enables us to take advantage of the simple gradient-based algorithms but leads to the inconsistency of the model results among parallel model runs. Second, the model has higher computational complexity as compared to the tensor regression models due to its Gaussian Process formulation. A more efficient computational algorithm might need to be derived to handle larger datasets.

## References

- [1] Alvaro Barbero and Suvrit Sra. Modular Proximal Optimization for Multidimensional Total-Variation Regularization. *Journal of Machine Learning Research*, 19(1):2232–2313, 2018.
- [2] Monica G Bobra and Sebastien Couvidat. Solar Flare Prediction using SDO/HMI Vector Magnetic Field Data with a Machine-Learning Algorithm. *The Astrophysical Journal*, 798(2):135, 2015.
- [3] Elynn Y Chen, Dong Xia, Chencheng Cai, and Jianqing Fan. Semiparametric Tensor Factor Analysis by Iteratively Projected SVD. *arXiv preprint arXiv:2007.02404*, 2020.
- [4] Yang Chen, Ward B Manchester, Alfred O Hero, Gabor Toth, Benoit DuFumier, Tian Zhou, Xiantong Wang, Haonan Zhu, Zeyu Sun, and Tamas I Gombosi. Identifying Solar Flare Precursors using Time Series of SDO/HMI Images and SHARP Parameters. *Space Weather*, 17(10):1404–1426, 2019.
- [5] Jerome Friedman, Trevor Hastie, Holger Höfling, and Robert Tibshirani. Pathwise Coordinate Optimization. *The Annals of Applied Statistics*, 1(2):302–332, 2007.
- [6] Weiwei Guo, Irene Kotsia, and Ioannis Patras. Tensor Learning for Regression. *IEEE Transactions on Image Processing*, 21(2):816–827, 2011.
- [7] Botao Hao, Boxiang Wang, Pengyuan Wang, Jingfei Zhang, Jian Yang, and Will Wei Sun. Sparse Tensor Additive Regression. *Journal of machine learning research*, 22, 2021.
- [8] Nan-Jung Hsu, Hsin-Cheng Huang, and Ruey S Tsay. Matrix Autoregressive Spatio-Temporal Models. *Journal of Computational and Graphical Statistics*, 30(4):1143–1155, 2021.
- [9] Hung Hung and Chen-Chien Wang. Matrix Variate Logistic Regression Model with Application to EEG Data. *Biostatistics*, 14(1):189–202, 2013.
- [10] Zhenbang Jiao, Hu Sun, Xiantong Wang, Ward Manchester, Tamas Gombosi, Alfred Hero, and Yang Chen. Solar Flare Intensity Prediction with Machine Learning Models. *Space Weather*, 18(7):e2020SW002440, 2020.
- [11] Álvaro Barbero Jiménez and Suvrit Sra. Fast Newton-Type Methods for Total Variation Regularization. In *International Conference on Machine Learning*, 2011.
- [12] Jian Kang, Brian J Reich, and Ana-Maria Staicu. Scalar-on-Image Regression via the Soft-thresholded Gaussian Process. *Biometrika*, 105(1):165–184, 2018.
- [13] Diederik P Kingma and Max Welling. Auto-Encoding Variational Bayes. *arXiv preprint arXiv:1312.6114*, 2013.
- [14] Tamara G Kolda and Brett W Bader. Tensor Decompositions and Applications. *SIAM review*, 51(3):455–500, 2009.
- [15] Jean Kossaifi, Zachary C Lipton, Arinbjörn Kolbeinsson, Aran Khanna, Tommaso Furlanello, and Anima Anandkumar. Tensor Regression Networks. *Journal of Machine Learning Research*, 21(1):4862–4882, 2020.
- [16] James R. Lemen, Alan M. Title, David J. Akin, Paul F. Boerner, Catherine Chou, Jerry F. Drake, Dexter W. Duncan, Christopher G. Edwards, Frank M. Friedlaender, Gary F. Heyman, Neal E. Hurlburt, Noah L. Katz, Gary D. Kushner, Michael Levay, Russell W. Lindgren, Dnyanesh P. Mathur, Edward L. McFeaters, Sarah Mitchell, Roger A. Rehse, Carolus J. Schrijver, Larry A. Springer, Robert A. Stern, Theodore D. Tarbell, Jean-Pierre Wuelser, C. Jacob Wolfson, Carl Yanari, Jay A. Bookbinder, Peter N. Cheimets, David Caldwell, Edward E. Deluca, Richard Gates, Leon Golub, Sang Park, William A. Podgorski, Rock I. Bush, Philip H. Scherrer, Mark A. Gummin, Peter Smith, Gary Auker, Paul Jerram, Peter Pool, Regina Soufli, David L. Windt, Sarah Beardsley, Matthew Clapp, James Lang, and Nicholas Waltham. The Atmospheric Imaging Assembly (AIA) on the Solar Dynamics Observatory (SDO). *Solar Physics*, 275(1-2):17–40, January 2012.
- [17] Xiaoshan Li, Da Xu, Hua Zhou, and Lexin Li. Tucker Tensor Regression and Neuroimaging Analysis. *Statistics in Biosciences*, 10(3):520–545, 2018.

- [18] Eric F Lock, Katherine A Hoadley, James Stephen Marron, and Andrew B Nobel. Joint and Individual Variation Explained (jive) for Integrated Analysis of Multiple Data Types. *The Annals of Applied Statistics*, 7(1):523, 2013.
- [19] Georgia Papadogeorgou, Zhengwu Zhang, and David B Dunson. Soft Tensor Regression. *Journal of Machine Learning Research*, 22:219–1, 2021.
- [20] Leonid I Rudin, Stanley Osher, and Emad Fatemi. Nonlinear Total Variation based Noise Removal Algorithms. *Physica D: nonlinear phenomena*, 60(1-4):259–268, 1992.
- [21] P. H. Scherrer, J. Schou, R. I. Bush, A. G. Kosovichev, R. S. Bogart, J. T. Hoeksema, Y. Liu, T. L. Duvall, J. Zhao, A. M. Title, C. J. Schrijver, T. D. Tarbell, and S. Tomczyk. The Helioseismic and Magnetic Imager (HMI) Investigation for the Solar Dynamics Observatory (SDO). *Solar Physics*, 275(1-2):207–227, January 2012.
- [22] Carolus J Schrijver. A Characteristic Magnetic Field Pattern Associated with All Major Solar Flares and its Use in Flare Forecasting. *The Astrophysical Journal*, 655(2):L117, 2007.
- [23] Hu Sun, Ward Manchester IV, and Yang Chen. Improved and Interpretable Solar Flare Predictions with Spatial and Topological Features of the Polarity Inversion Line Masked Magnetograms. *Space Weather*, 19(12):e2021SW002837, 2021.
- [24] Zeyu Sun, Monica G Bobra, Xiantong Wang, Yu Wang, Hu Sun, Tamas Gombosi, Yang Chen, and Alfred Hero. Predicting Solar Flares using CNN and LSTM on Two Solar Cycles of Active Region Data. *The Astrophysical Journal*, 931(2):163, 2022.
- [25] Robert Tibshirani, Michael Saunders, Saharon Rosset, Ji Zhu, and Keith Knight. Sparsity and Smoothness via the Fused Lasso. *Journal of the Royal Statistical Society: Series B (Statistical Methodology)*, 67(1):91–108, 2005.
- [26] Ryan J Tibshirani. Adaptive Piecewise Polynomial Estimation via Trend Filtering. *The Annals of Statistics*, 42(1):285–323, 2014.
- [27] Xiantong Wang, Yang Chen, Gabor Toth, Ward B Manchester, Tamas I Gombosi, Alfred O Hero, Zhenbang Jiao, Hu Sun, Meng Jin, and Yang Liu. Predicting Solar Flares with Machine Learning: Investigating Solar Cycle Dependence. *The Astrophysical Journal*, 895(1):3, 2020.
- [28] Xiao Wang, Hongtu Zhu, and Alzheimer’s Disease Neuroimaging Initiative. Generalized Scalar-on-Image Regression Models via Total Variation. *Journal of the American Statistical Association*, 112(519):1156–1168, 2017.
- [29] Christopher KI Williams and Carl Edward Rasmussen. *Gaussian Processes for Machine Learning*, volume 2. MIT press Cambridge, MA, 2006.
- [30] Rose Yu, Guangyu Li, and Yan Liu. Tensor Regression meets Gaussian Processes. In *International Conference on Artificial Intelligence and Statistics*, pages 482–490. PMLR, 2018.
- [31] Hua Zhou and Lexin Li. Regularized Matrix Regression. *Journal of the Royal Statistical Society: Series B (Statistical Methodology)*, 76(2):463–483, 2014.
- [32] Hua Zhou, Lexin Li, and Hongtu Zhu. Tensor Regression with Applications in Neuroimaging Data Analysis. *Journal of the American Statistical Association*, 108(502):540–552, 2013.

## A Proof of Lemma 2.1

The anisotropic total variation penalty can be simplified as follows, thanks to the rank-1 assumption on the feature map  $\mathcal{W}_{s,t}$ :

$$\|\mathcal{W}_{s,t}\|_{\text{TV}} = \sum_{i=1}^{H-1} \sum_{j=1}^W |\mathcal{W}_{s,t}(i+1, j) - \mathcal{W}_{s,t}(i, j)| + \sum_{i=1}^H \sum_{j=1}^{W-1} |\mathcal{W}_{s,t}(i, j+1) - \mathcal{W}_{s,t}(i, j)| \quad (18)$$

$$= \sum_{i=1}^{H-1} \sum_{j=1}^W |A(s, i+1) - A(s, i)| \cdot |B(t, j)| + \sum_{i=1}^H \sum_{j=1}^{W-1} |B(t, j+1) - B(t, j)| \cdot |A(s, i)| \quad (19)$$

As a result, the total variation penalty has an elegant multiplicative formulation:

$$\begin{aligned} \lambda \sum_{s=1}^h \sum_{t=1}^w \|\mathcal{W}_{s,t}\|_{\text{TV}} &= \left( \lambda \sum_{t=1}^w \sum_{j=1}^W |B(t, j)| \right) \cdot \left( \sum_{s=1}^h \sum_{i=1}^{H-1} |A(s, i+1) - A(s, i)| \right) \\ &\quad + \left( \lambda \sum_{t=1}^w \sum_{j=1}^{W-1} |B(t, j+1) - B(t, j)| \right) \cdot \left( \sum_{s=1}^h \sum_{i=1}^H |A(s, i)| \right) \\ &= (\lambda \cdot \|B\|_1) \cdot \|\nabla_x A\|_1 + (\lambda \cdot \|B\|_1) \cdot \|A\|_1 \end{aligned} \quad (20)$$

where  $\nabla_x$  is the horizontal (i.e. row) first-order derivative operator and  $\|\cdot\|_1$  is the  $\ell_1$  norm. (20) turns out to be a fused-lasso type penalty [25] with both a penalty on the sparsity of  $A$  and a penalty on the smoothness of each row of  $A$ . This leads to a rank-1 feature map with smoothness. Different from the fused lasso penalty, we only introduce one tuning parameter  $\lambda$  and it is re-weighted by the smoothness and sparsity of  $B$  when one is updating  $A$ , and vice versa.

## B Proximal Gradient Descent Algorithm for Tensor-GPST

Given the factorization assumption for the tensor multi-linear kernel factors  $K_1, K_2, K_3$ :

$$K_1 = U_1^\top U_1, K_2 = U_2^\top U_2, K_3 = U_3^\top U_3 \quad (21)$$

where  $U_1 \in \mathbb{R}^{r_1 \times h}, U_2 \in \mathbb{R}^{r_2 \times w}, U_3 \in \mathbb{R}^{r_3 \times C}$ . One can rewrite the penalized negative log-likelihood loss function in (14) as:

$$\begin{aligned} \min_{A, B, U_{1:3}, \sigma} L &= \frac{1}{2} \log |\tilde{\mathbf{U}} \tilde{\mathbf{U}}^\top + \mathbf{D}_\sigma| + \frac{1}{2} \mathbf{y}^\top (\tilde{\mathbf{U}} \tilde{\mathbf{U}}^\top + \mathbf{D}_\sigma)^{-1} \mathbf{y} \\ &\quad + \lambda \sum_{s=1}^h \sum_{t=1}^w \left\{ \sum_{i=1}^{H-1} \sum_{j=1}^W |\mathcal{W}_{s,t}(i+1, j) - \mathcal{W}_{s,t}(i, j)| + \sum_{i=1}^H \sum_{j=1}^{W-1} |\mathcal{W}_{s,t}(i, j+1) - \mathcal{W}_{s,t}(i, j)| \right\} \\ &= \ell(A, B, U_{1:3}, \sigma) + \lambda \sum_{s=1}^h \sum_{t=1}^w \|\mathcal{W}_{s,t}\|_{\text{TV}} \end{aligned} \quad (22)$$

and we update the model parameters via a block coordinate descent scheme following the order of:  $A \rightarrow B \rightarrow (U_1, U_2, U_3) \rightarrow \sigma \rightarrow A \rightarrow B \rightarrow \dots$

The derivation of the gradients of  $\ell(\cdot)$  w.r.t.  $A, B, U_{1:3}, \sigma$  have been made trivial thanks to the factorization assumption. For the  $(i, j)$ -th element of  $A$ , for instance, we have its partial derivative as:

$$\frac{\partial \ell}{\partial A}(i, j) = \text{tr} \left[ \left( \frac{\partial \ell}{\partial \tilde{\mathbf{U}}} \right)^\top \left( \frac{\partial \tilde{\mathbf{U}}}{\partial A(i, j)} \right) \right], \quad \frac{\partial \tilde{\mathbf{U}}}{\partial A(i, j)} = \mathcal{X}^\top (\mathbf{I}_C \otimes B \otimes \mathbf{O}_{ij})^\top (U_3 \otimes U_2 \otimes U_1)^\top$$

where  $\mathbf{O}_{ij} \in \mathbb{R}^{h \times H}$  is a matrix with all entries being zero except the  $(i, j)$ -th entry being one. The derivative of  $\ell$  w.r.t.  $\tilde{\mathbf{U}}$  has an explicit form [30]:

$$\frac{\partial \ell}{\partial \tilde{\mathbf{U}}} = \tilde{\mathbf{U}} \left( \Sigma^{-1} + \Sigma^{-1} \tilde{\mathbf{U}}^\top \mathbf{y} \mathbf{D}_\sigma^{-1} \mathbf{y}^\top \tilde{\mathbf{U}} \Sigma^{-1} \right) - \mathbf{y} \mathbf{D}_\sigma^{-1} \mathbf{y}^\top \tilde{\mathbf{U}} \Sigma^{-1}$$

where  $\Sigma = \mathbf{D}_\sigma + \tilde{\mathbf{U}}^\top \tilde{\mathbf{U}}$ . The derivative of  $\tilde{\mathbf{U}}$  w.r.t.  $A, B, U_1, U_2, U_3$  can be readily derived by simply replacing each matrix parameter with a sparse binary matrix such as  $\mathbf{O}_{ij}$  stated above. For example for  $U_2$ , one has:

$$\frac{\partial \tilde{\mathbf{U}}}{\partial U_2(i,j)} = \mathcal{X}^\top (\mathbf{I}_C \otimes B \otimes A)^\top (U_3 \otimes \mathbf{O}_{ij} \otimes U_1)^\top$$

where  $\mathbf{O}_{ij} \in \mathbb{R}^{r_2 \times w}$  and is sparse except the  $(i,j)$ -th element being one. The gradients for  $U_1, U_2, U_3$  can be used for parameter update, and for  $A$  and  $B$ , we consider updating them via proximal gradient descent. For  $A$  at the  $k$ -th iteration, for example, one applies the gradient descent to get an estimate proposal:  $\hat{A}^{(k+\frac{1}{2})} = \hat{A}^{(k)} - \eta_k \frac{\partial \ell}{\partial A}$ , and then solves the following optimization problem, which is commonly known as the proximal step:

$$\text{prox}_{\text{TV}}(\hat{A}^{(k+\frac{1}{2})}) = \arg \min_A \left\{ \frac{1}{2\eta_k} \|A - \hat{A}^{(k+\frac{1}{2})}\|_F^2 + \lambda \sum_{s=1}^h \sum_{t=1}^w \|\mathcal{W}_{s,t}\|_{\text{TV}} \right\} \quad (23)$$

where  $\eta_k$  is the learning rate of the current iterative step.

Solving the proximal problem in (23) can be broken down into multiple parallel 1-D *fused lasso signal approximation* problem. According to Proposition 1 of [5], solving (23) can be further broken down into first solving  $h$  total variation de-noising problem [20]:

$$\tilde{A}(s,:) \leftarrow \arg \min_{\alpha \in \mathbb{R}^H} \frac{1}{2\eta_k} \left\| \alpha - \hat{A}^{(k+\frac{1}{2})}(s,:)\right\|_F^2 + (\lambda \cdot \|B\|_1) \cdot \sum_{i=2}^H |\alpha_{i+1} - \alpha_i|, \quad s = 1, 2, \dots, h \quad (24)$$

Then one can apply a soft-thresholding operator  $\mathcal{S}_{\lambda \|\nabla_x B\|_1}(\cdot)$ , element-wisely, to  $\tilde{A} := \text{prox}_{\text{TV}}(\hat{A}^{(k+\frac{1}{2})})$  to obtain the penalized solution for (23). The problem in (24) can be efficiently solved via the python implementation in prox-TV based on a fast Newton's method [11, 1]. Similar technique can be applied to update  $B$ , and therefore the final optimization algorithm consists of both a gradient descent step and a fused-lasso proximal step. A more general theoretical discussion on the total variation penalty over 1-D signals can be found in [26].

The gradient of  $\ell$  w.r.t.  $\sigma$  (or  $\sigma^2$ ) can be easily derived as follows:

$$\frac{\partial \ell}{\partial \sigma^2} = \text{tr} \left[ \left( \frac{\partial \ell}{\partial (\mathbf{K} + \mathbf{D}_\sigma)^{-1}} \right)^\top \left( \frac{\partial (\mathbf{K} + \mathbf{D}_\sigma)^{-1}}{\partial \sigma^2} \right) \right] = \text{tr} \left[ \frac{1}{2} (\mathbf{K} + \mathbf{D}_\sigma)^{-1} - \frac{1}{2} (\mathbf{K} + \mathbf{D}_\sigma)^{-2} \mathbf{y} \mathbf{y}^\top \right] \quad (25)$$

Predictions on the unseen testing data with covariates  $\mathbf{X}_*$ , given the training data  $(\mathbf{X}, \mathbf{y})$ , can be easily derived using the predictive distribution  $(\mathbf{y}_* | \mathbf{X}_*, \mathbf{X}, \mathbf{y}) \sim \mathcal{N}(\boldsymbol{\mu}_*, \boldsymbol{\Sigma}_*)$ :

$$\begin{aligned} \boldsymbol{\mu}_* &= \hat{\mathcal{K}}(\mathbf{X}_*, \mathbf{X}) \left( \hat{\mathcal{K}}(\mathbf{X}, \mathbf{X}) + \mathbf{D}_{\hat{\sigma}} \right)^{-1} \mathbf{y} \\ \boldsymbol{\Sigma}_* &= \hat{\mathcal{K}}(\mathbf{X}_*, \mathbf{X}_*) + \mathbf{D}_{\hat{\sigma}} - \hat{\mathcal{K}}(\mathbf{X}_*, \mathbf{X}) \left( \hat{\mathcal{K}}(\mathbf{X}, \mathbf{X}) + \mathbf{D}_{\hat{\sigma}} \right)^{-1} \hat{\mathcal{K}}(\mathbf{X}_*, \mathbf{X})^\top \end{aligned}$$

where  $\hat{\mathcal{K}}(\cdot, \cdot)$  is the kernel function in (8) but evaluated at the estimated model parameters, and  $\hat{\mathcal{K}}(\mathbf{X}_*, \mathbf{X})$  simply denotes the covariances between the unseen data  $\mathbf{X}_*$  and the training data  $\mathbf{X}$ , and the other notations follow.

## C Proof of Theorem 2.2

The proof of Theorem 2.2 is largely based on the convergence results of proximal gradient descent but with additional consideration on the alternating descent scheme. We denote an arbitrary collection of model parameters as  $\theta := (A, B, U_{1:3}, \sigma)$ . Since we update the four blocks of parameters cyclically in Algorithm 1, within each iteration, we further denote the intermediate parameter updates as  $\hat{\theta}^{(k)} \xrightarrow{\text{update } A} \hat{\theta}^{(k+\frac{1}{4})} \xrightarrow{\text{update } B} \hat{\theta}^{(k+\frac{1}{2})} \xrightarrow{\text{update } U_{1:3}} \hat{\theta}^{(k+\frac{3}{4})} \xrightarrow{\text{update } \sigma} \hat{\theta}^{(k+1)}$ . In the remainder of the proof, we will use  $U$  to denote  $U_{1:3}$ .

In order to show the upper bound of the difference of the loss function after  $K$  iterations with its global minimum  $L(\theta^*)$ , we first show Lemma C.1:

**Lemma C.1.** Given the alternating proximal gradient descent algorithm in Algorithm 1 and the assumptions made in Theorem 2.2, one can bound  $L(\widehat{\theta}^{(k+\frac{v}{4})})$ ,  $v \in \{1, 2, 3, 4\}$  as:

$$L(\widehat{\theta}^{(k+\frac{1}{4})}) \leq L(A^*, \widehat{B}^{(k)}, \widehat{U}^{(k)}, \widehat{\sigma}^{(k)}) + \frac{1}{2\alpha} \left\{ \left\| \widehat{A}^{(k)} - A^* \right\|^2 - \left\| \widehat{A}^{(k+1)} - A^* \right\|^2 \right\} \quad (26)$$

$$L(\widehat{\theta}^{(k+\frac{1}{2})}) \leq L(\widehat{A}^{(k+1)}, B^{(*)}, \widehat{U}^{(k)}, \widehat{\sigma}^{(k)}) + \frac{1}{2\alpha} \left\{ \left\| \widehat{B}^{(k)} - B^* \right\|^2 - \left\| \widehat{B}^{(k+1)} - B^* \right\|^2 \right\} \quad (27)$$

$$L(\widehat{\theta}^{(k+\frac{3}{4})}) \leq L(\widehat{A}^{(k+1)}, \widehat{B}^{(k+1)}, U^*, \widehat{\sigma}^{(k)}) + \frac{1}{2\alpha} \left\{ \left\| \widehat{U}^{(k)} - U^* \right\|^2 - \left\| \widehat{U}^{(k+1)} - U^* \right\|^2 \right\} \quad (28)$$

$$L(\widehat{\theta}^{(k+1)}) \leq L(\widehat{A}^{(k+1)}, \widehat{B}^{(k+1)}, \widehat{U}^{(k+1)}, \sigma^*) + \frac{1}{2\alpha} \left\{ \left\| \widehat{\sigma}^{(k)} - \sigma^* \right\|^2 - \left\| \widehat{\sigma}^{(k+1)} - \sigma^* \right\|^2 \right\} \quad (29)$$

*Proof.* It suffices to prove (26), and the rest of the bounds follow the same technique.

First, given that the gradient of  $\ell(\cdot)$  w.r.t. to  $A$  is Lipschitz continuous with constant  $M_A$ , i.e.  $\|\nabla_A \ell(A_1) - \nabla_A \ell(A_2)\| \leq M_A \|A_1 - A_2\|, \forall A_1, A_2$ . Since the other parameters also share the same property but have different Lipschitz constant  $M_B, M_U, M_\sigma$ , we use  $M := \max\{M_A, M_B, M_U, M_\sigma\}$  for all parameters. Given the Lipschitz continuity of the derivative, one has:

$$\ell(\widehat{\theta}^{(k+\frac{1}{4})}) \leq \ell(\widehat{\theta}^{(k)}) + \langle \nabla_A \ell(\widehat{\theta}^{(k)}), \widehat{A}^{(k+1)} - \widehat{A}^{(k)} \rangle + \frac{M}{2} \|\widehat{A}^{(k+1)} - \widehat{A}^{(k)}\|^2 \quad (30)$$

which is a direct result from the following inequality for any function  $\ell(\cdot)$  with  $M$ -Lipschitz continuous derivative:

$$\ell(y) \leq \ell(x) + \langle \nabla_x \ell(x), y - x \rangle + \frac{M}{2} \|y - x\|^2$$

Additionally, since  $\ell(\cdot)$  is assumed as block-wise convex, one has a natural upper bound of  $\ell(\widehat{\theta}^{(k)})$  based on convexity:

$$\ell(\widehat{\theta}^{(k)}) \leq \ell(A^*, \widehat{B}^{(k)}, \widehat{U}^{(k)}, \widehat{\sigma}^{(k)}) - \langle \nabla_A \ell(\widehat{\theta}^{(k)}), A^* - \widehat{A}^{(k)} \rangle \quad (31)$$

Combining (30) and (31), one obtains:

$$\ell(\widehat{\theta}^{(k+\frac{1}{4})}) \leq \ell(A^*, \widehat{B}^{(k)}, \widehat{U}^{(k)}, \widehat{\sigma}^{(k)}) + \langle \nabla_A \ell(\widehat{\theta}^{(k)}), \widehat{A}^{(k+1)} - A^* \rangle + \frac{M}{2} \|\widehat{A}^{(k+1)} - \widehat{A}^{(k)}\|^2 \quad (32)$$

Also, since  $\widehat{A}^{(k+1)}$  is obtained via a proximal step:

$$\widehat{A}^{(k+1)} = \arg \min_A \frac{1}{2\alpha} \left\| A - \left( \widehat{A}^{(k)} - \alpha \nabla_A \ell(\widehat{\theta}^{(k)}) \right) \right\|^2 + \lambda R(A, \widehat{B}^{(k)})$$

$\widehat{A}^{(k+1)}$  should satisfy the following subgradient condition:

$$G_\alpha(\widehat{\theta}^{(k)}) - \nabla_A \ell(\widehat{\theta}^{(k)}) \in \lambda \cdot \partial_A R\left(\widehat{A}^{(k+1)}, \widehat{B}^{(k)}\right) \quad (33)$$

where  $G_\alpha(\widehat{\theta}^{(k)}) := -\frac{1}{\alpha} (\widehat{A}^{(k+1)} - \widehat{A}^{(k)})$  is the proximal gradient. Using the definition of subgradient, one can achieve a trivial inequality as follows:

$$\lambda R\left(\widehat{A}^{(k+1)}, \widehat{B}^{(k)}\right) + \langle G_\alpha(\widehat{\theta}^{(k)}) - \nabla_A \ell(\widehat{\theta}^{(k)}), A^* - \widehat{A}^{(k+1)} \rangle \leq \lambda R\left(A^*, \widehat{B}^{(k)}\right) \quad (34)$$

Combining (32) and (34), we have:

$$\begin{aligned}
L(\widehat{\theta}^{(k+\frac{1}{4})}) &= \ell(\widehat{\theta}^{(k+\frac{1}{4})}) + \lambda R\left(\widehat{A}^{(k+1)}, \widehat{B}^{(k)}\right) \\
&\leq L(A^*, \widehat{B}^{(k)}, \widehat{U}^{(k)}, \widehat{\sigma}^{(k)}) + \left\langle G_\alpha(\widehat{\theta}^{(k)}), \widehat{A}^{(k+1)} - A^* \right\rangle + \frac{M}{2} \|\widehat{A}^{(k+1)} - \widehat{A}^{(k)}\|^2 \\
&\leq L(A^*, \widehat{B}^{(k)}, \widehat{U}^{(k)}, \widehat{\sigma}^{(k)}) + \left\langle G_\alpha(\widehat{\theta}^{(k)}), \widehat{A}^{(k)} - \alpha G_\alpha(\widehat{\theta}^{(k)}) - A^* \right\rangle + \frac{1}{2\alpha} \|\alpha G_\alpha(\widehat{\theta}^{(k)})\|^2 \\
&= L(A^*, \widehat{B}^{(k)}, \widehat{U}^{(k)}, \widehat{\sigma}^{(k)}) + \frac{1}{2\alpha} \left\{ \|\widehat{A}^{(k)} - A^*\|^2 - \|\widehat{A}^{(k+1)} - A^*\|^2 \right\}
\end{aligned}$$

which completes the proof.  $\square$

In the classical proximal gradient descent context, where one updates a single parameter iteratively, the bound in Lemma C.1 leads to a convergence rate of the algorithm at  $\mathcal{O}(1/K)$ , after one adds up all the inequalities from iteration 1 to  $K$ . The key difference is that, on the right hand side of the inequality (26), the loss function is evaluated at the global minima of  $A$  and the value of  $B, U, \sigma$  at the  $k$ -th iteration. We need to quantify the gap between  $L(A^*, \widehat{B}^{(k)}, \widehat{U}^{(k)}, \widehat{\sigma}^{(k)})$  and  $L(\theta^*)$  to reach the final error bound result and this gap is shown in Lemma C.2.

**Lemma C.2.** *The difference of  $L(A^*, \widehat{B}^{(k)}, \widehat{U}^{(k)}, \widehat{\sigma}^{(k)})$  and  $L(\theta^*) := L(A^*, B^*, U^*, \sigma^*)$  can be fully characterized as:*

$$L(A^*, \widehat{B}^{(k)}, \widehat{U}^{(k)}, \widehat{\sigma}^{(k)}) - L(\theta^*) \leq \frac{M}{2} \left\{ \|\widehat{B}^{(k)} - B^*\| + \|\widehat{U}^{(k)} - U^*\| + \|\widehat{\sigma}^{(k)} - \sigma^*\| \right\}^2 \quad (35)$$

$$+ \|\nabla_B \ell(\theta^*)\| \cdot \|\widehat{B}^{(k)} - B^*\| + \lambda R\left(A^*, \widehat{B}^{(k)} - B^*\right) \quad (36)$$

where (35) is the additional loss incurred by using the iterative value of the other parameters instead of the global optimum (ALT-gap), and (36) is the additional loss incurred by using the total variation penalty with the  $k$ -th iterative value of  $B$  (TV-gap).

*Proof.* We start the derivation with the following trivial decomposition:

$$L(A^*, \widehat{B}^{(k)}, \widehat{U}^{(k)}, \widehat{\sigma}^{(k)}) - L(\theta^*) = L(A^*, \widehat{B}^{(k)}, \widehat{U}^{(k)}, \widehat{\sigma}^{(k)}) - L(A^*, B^*, \widehat{U}^{(k)}, \widehat{\sigma}^{(k)}) \quad (37)$$

$$+ L(A^*, B^*, \widehat{U}^{(k)}, \widehat{\sigma}^{(k)}) - L(A^*, B^*, U^*, \widehat{\sigma}^{(k)}) \quad (38)$$

$$+ L(A^*, B^*, U^*, \widehat{\sigma}^{(k)}) - L(\theta^*) \quad (39)$$

We need to bound (37), (38) and (39) separately. For (37), we have:

$$\begin{aligned}
&L(A^*, \widehat{B}^{(k)}, \widehat{U}^{(k)}, \widehat{\sigma}^{(k)}) - L(A^*, B^*, \widehat{U}^{(k)}, \widehat{\sigma}^{(k)}) \\
&= \ell(A^*, \widehat{B}^{(k)}, \widehat{U}^{(k)}, \widehat{\sigma}^{(k)}) - \ell(A^*, B^*, \widehat{U}^{(k)}, \widehat{\sigma}^{(k)}) + \lambda R\left(A^*, \widehat{B}^{(k)} - B^*\right) \\
&\leq \left\langle \nabla_B \ell(A^*, B^*, \widehat{U}^{(k)}, \widehat{\sigma}^{(k)}), \widehat{B}^{(k)} - B^* \right\rangle + \frac{M}{2} \|\widehat{B}^{(k)} - B^*\|^2 + \lambda R\left(A^*, \widehat{B}^{(k)} - B^*\right) \\
&\leq \|\widehat{B}^{(k)} - B^*\| \cdot \left( \|\nabla_B \ell(\theta^*)\| + M \|\widehat{U}^{(k)} - U^*\| + M \|\widehat{\sigma}^{(k)} - \sigma^*\| \right) + \frac{M}{2} \|\widehat{B}^{(k)} - B^*\|^2 + \lambda R\left(A^*, \widehat{B}^{(k)} - B^*\right)
\end{aligned} \quad (40)$$

where the last line follows from the Cauchy-Schwartz inequality followed by the Lipschitz continuity of the gradient and the triangle inequality of the Frobenius norm.

As for (38), similar technique follows and lead to:

$$\begin{aligned}
L(A^*, B^*, \widehat{U}^{(k)}, \widehat{\sigma}^{(k)}) - L(A^*, B^*, U^*, \widehat{\sigma}^{(k)}) &= \ell(A^*, B^*, \widehat{U}^{(k)}, \widehat{\sigma}^{(k)}) - \ell(A^*, B^*, U^*, \widehat{\sigma}^{(k)}) \\
&\leq \left\langle \nabla_U \ell(A^*, B^*, U^*, \widehat{\sigma}^{(k)}), \widehat{U}^{(k)} - U^* \right\rangle + \frac{M}{2} \|\widehat{U}^{(k)} - U^*\|^2 \\
&\leq M \|\widehat{U}^{(k)} - U^*\| \cdot \|\widehat{\sigma}^{(k)} - \sigma^*\| + \frac{M}{2} \|\widehat{U}^{(k)} - U^*\|^2
\end{aligned}$$

where the last line uses the fact that at the global optimum, we have  $\nabla_U \ell(\theta^*) = 0$ .

Similarly for (39), one has:

$$L(A^*, B^*, U^*, \hat{\sigma}^{(k)}) - L(\theta^*) \leq \left\langle \nabla_{\sigma} \ell(\theta^*), \hat{\sigma}^{(k)} - \sigma^* \right\rangle + \frac{M}{2} \|\hat{\sigma}^{(k)} - \sigma^*\|^2$$

Combining the three individual upper bounds together yields the result and thereby completes the proof.  $\square$

Similar results in Lemma C.2 can be easily derived for the other three parameters other than  $A^*$ . With these theoretical results, we are now ready to prove Theorem 2.2.

*Proof.* Combining the results in Lemma C.1 and C.2, we have the following upper bound for  $L(\hat{\theta}^{(k+\frac{1}{4})}) - L(\theta^*)$ :

$$\begin{aligned} L(\hat{\theta}^{(k+\frac{1}{4})}) - L(\theta^*) &\leq \frac{M}{2} \left\{ \|\hat{B}^{(k)} - B^*\| + \|\hat{U}^{(k)} - U^*\| + \|\hat{\sigma}^{(k)} - \sigma^*\| \right\}^2 \\ &\quad + \|\nabla_B \ell(\theta^*)\| \cdot \|\hat{B}^{(k)} - B^*\| + \lambda R(A^*, \hat{B}^{(k)} - B^*) \\ &\quad + \frac{1}{2\alpha} \left\{ \|\hat{A}^{(k)} - A^*\|^2 - \|\hat{A}^{(k+1)} - A^*\|^2 \right\} \end{aligned}$$

If  $B, U, \sigma$  is fixed at their global minimum and one only updates  $A$  via proximal gradient descent, the error bound here vanishes to the last term and can be further reduced if one adds up the inequality from iteration 1 to  $K$ , leading to the classical proximal gradient descent convergence rate result. Similar bounds for  $L(\hat{\theta}^{(k+\frac{1}{2})}), L(\hat{\theta}^{(k+\frac{3}{4})}), L(\hat{\theta}^{(k+1)})$  can be derived and we aggregate the results together as follows:

$$\begin{aligned} \sum_{k=0}^K \sum_{v=1}^4 \left( L(\hat{\theta}^{(k+\frac{v}{4})}) - L(\theta^*) \right) &\leq \frac{1}{2\alpha} \left\{ \|\hat{\theta}^{(0)} - \theta^*\|^2 - \|\hat{\theta}^{(K)} - \theta^*\|^2 \right\} \\ &\quad + \sum_{k=0}^K h_{\lambda}(\hat{A}^{(k+1)} - A^*, \hat{B}^{(k+1)} - B^*, \hat{B}^{(k)} - B^*) \\ &\quad + \frac{1}{2\alpha} \sum_{k=0}^K \tau(\hat{\theta}^{(k+1)}, \hat{\theta}^{(k)}, \theta^*) \end{aligned} \tag{41}$$

where  $h_{\lambda}(\hat{A}^{(k+1)} - A^*, \hat{B}^{(k+1)} - B^*, \hat{B}^{(k)} - B^*)$  is the extra gap from the optimal loss created by the existence of the total variation penalty in the loss function (TV-gap) and is defined as:

$$\begin{aligned} h_{\lambda}(\hat{A}^{(k+1)} - A^*, \hat{B}^{(k+1)} - B^*, \hat{B}^{(k)} - B^*) &:= 3\|\nabla_A \ell(\theta^*)\| \cdot \|\hat{A}^{(k+1)} - A^*\| + 2\|\nabla_B \ell(\theta^*)\| \cdot \|\hat{B}^{(k+1)} - B^*\| \\ &\quad + \|\nabla_B \ell(\theta^*)\| \cdot \|\hat{B}^{(k)} - B^*\| + \lambda R(A^*, \hat{B}^{(k)} - B^*) \\ &\quad + 3\lambda R(\hat{A}^{(k+1)} - A^*, B^*) + 2\lambda R(A^*, \hat{B}^{(k+1)} - B^*) \\ &\quad + 2\lambda R(\hat{A}^{(k+1)} - A^*, \hat{B}^{(k+1)} - B^*) \end{aligned} \tag{42}$$

where  $R(A, B)$  is the total variation penalty defined in Lemma 2.1.  $\tau(\hat{\theta}^{(k+1)}, \hat{\theta}^{(k)}, \theta^*)$  is the extra gap from the optimal loss created by the usage of iterative value of the parameters during the alternating proximal gradient descent (ALT-gap) and is defined as:

$$\begin{aligned} \tau(\hat{\theta}^{(k+1)}, \hat{\theta}^{(k)}, \theta^*) &:= \left[ \|\hat{B}^{(k)} - B^*\| + \|\hat{U}^{(k)} - U^*\| + \|\hat{\sigma}^{(k)} - \sigma^*\| \right]^2 \\ &\quad + \left[ \|\hat{A}^{(k+1)} - A^*\| + \|\hat{U}^{(k)} - U^*\| + \|\hat{\sigma}^{(k)} - \sigma^*\| \right]^2 \\ &\quad + \left[ \|\hat{A}^{(k+1)} - A^*\| + \|\hat{B}^{(k+1)} - B^*\| + \|\hat{\sigma}^{(k)} - \sigma^*\| \right]^2 \\ &\quad + \left[ \|\hat{A}^{(k+1)} - A^*\| + \|\hat{B}^{(k+1)} - B^*\| + \|\hat{U}^{(k+1)} - U^*\| \right]^2 \end{aligned} \tag{43}$$

The final result can be derived from (41) by lower bounding the left hand side:

$$\sum_{k=0}^K \sum_{v=1}^4 \left( L(\hat{\theta}^{(k+\frac{v}{4})}) - L(\theta^*) \right) \geq 4(K+1) \left( L(\hat{\theta}^{(K+1)}) - L(\theta^*) \right)$$

which is evident given that each step is a descent step.  $\square$

Although we cannot fully verify the assumptions made, we plot the history of the loss function and the relative change of the model parameters for our real data application in Figure 6. Empirically, our model demonstrates a convergence rate at  $\mathcal{O}(1/K)$  (see the red curve fitted based on a polynomial model with function form  $\ell(k) = a + \frac{b}{c+k}$ ).

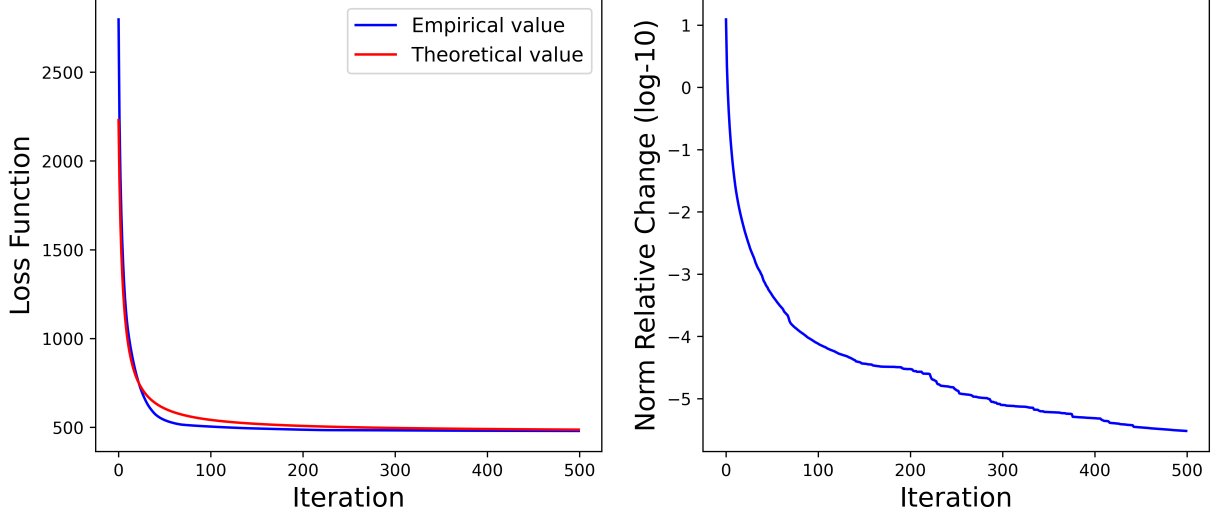


Figure 6: (Left) Loss history of the solar flare intensity regression task with Tensor-GPST ( $\lambda = 1.0$ ); A curve at the order of  $\mathcal{O}(1/K)$  is fitted to the loss history and empirically, the algorithm converges at the rate of  $\mathcal{O}(1/K)$  to a local minimum. (Right) History of the Frobenius norm of the relative change of model parameters in log-10 scale, which suggests that the parameters converge to a stationary point, and thus the ALT-gap and the TV-gap will converge to a constant.

## D Details of the Simulation Study

In this section we provide the details on generating the simulation data. Given the three types of data in Figure 2, we use two sparse and banded tensor contracting factors ( $A, B$ ) (see the top of Figure 7a) to contract each channel to a  $3 \times 3$  tensor (see Figure 1a about the contraction operation). ( $A, B$ ) in Figure 7a essentially do a  $5 \times 5$  block averaging for the four corners, four sides and the middle block of each channel data. So one can expect the Type 1 & 3 data to have its *signal* in the four corners of the contracted tensor, and Type 2 has its *signal* in the middle block. Given the contracted tensor, we use the multi-linear kernel, specified in Figure 7a (bottom) to generate the response variables via:

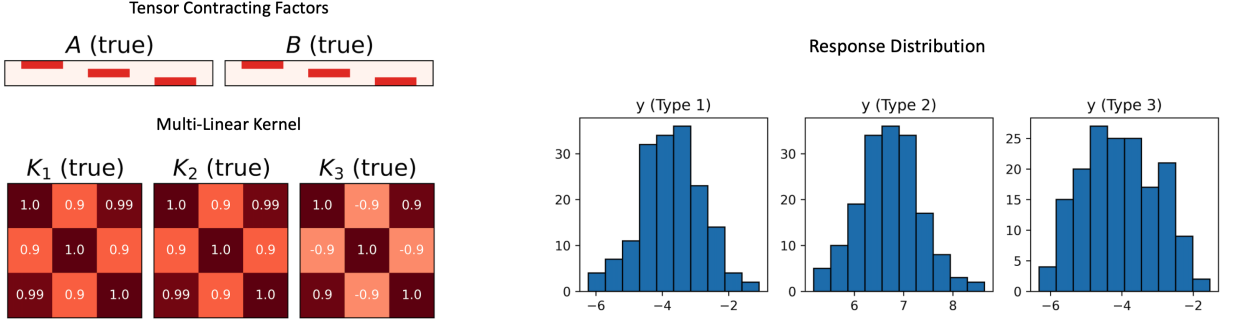
$$(y_1, \dots, y_N)^\top \sim \mathcal{N}(0, \mathbf{K}^* + \sigma^2 \mathbf{I})$$

where  $\mathbf{K}^*(i, j) = \text{vec}(\mathcal{X}_i)^\top [K_3 \otimes (B^\top K_2 B) \otimes (A^\top K_1 A)] \text{vec}(\mathcal{X}_j)$  and  $\sigma = 0.5$ .

One can notice from the kernel  $K_3$  that channel 1 & 3 are highly correlated and channel 2 is negatively correlated with both channel 1 & 3, and this is reflected in Figure 7b, where we plot the distribution of the simulated sample of size 500, by the data type. The tensor regression problem is to use the original  $25 \times 25 \times 3$  tensors  $\mathcal{X}_i$  to forecast the regression label  $y_i$ .

## E Details of the AIA-HMI Solar Flare Imaging Dataset

In this appendix, we provide some astrophysical backgrounds and additional details on data preprocessing about the AIA-HMI solar flare imaging datasets.



(a) True tensor contracting factors ( $A, B$ ) (top) and true multi-linear kernels (bottom).

(b) Distribution of the response variable  $y$  by type (see type definition in Figure 2. Total sample size  $N = 500$ .

Figure 7: Ground Truth of the Simulated data. (a) The true tensor contracting factors ( $A, B$ ) (top), where each has a banded structure with the 5 consecutive pixels filled with 0.2 on each row. The bottom shows the multi-linear kernel  $K_1, K_2, K_3$ . (b) The resulting response distribution of each type of data. One can see how type 1 & 3 has similar distribution, thanks to their high channel correlation in  $K_3$ .

There are over 12,000 solar flares recorded by the Geostationary Operational Environmental Satellite (GOES) from May, 2010 to June, 2017, with intensity at least at the A-class flare level (peak X-ray brightness  $< 10^{-7} \text{W/m}^2$ ). Among these flares, 4,409 are B-class flares ( $10^{-7} \sim 10^{-6} \text{W/m}^2$ ), 710 are M-class flares ( $10^{-5} \sim 10^{-4} \text{W/m}^2$ ) and 50 are X-class flares ( $> 10^{-4} \text{W/m}^2$ ). We combine the M-class and X-class flares in a single class, we name the class as M/X-class flares (referred to as M-class flare in the main paper). Each flare is associated with a solar active region, which is a localized, transient volume of the solar atmosphere characterized by complex magnetic fields. We collect the AIA and HMI imaging data for each of the M/X-class flare during this period, and collect the B-class flares happened within the same active regions to construct our own database. Given the data availability, we end up with a database of 1,264 B-class flares and 728 M/X-class flares.

The AIA imaging data has 8 channels, distinguished by the wavelength band of the Extreme Ultraviolet (EUV) and Ultraviolet (UV) spectrum used to image the Sun<sup>3</sup>. The AIA channels are named under their respective spectral band: AIA-94Å, AIA-131Å, AIA-171Å, AIA-193Å, AIA-211Å, AIA-304Å, AIA-335Å and AIA-1600Å. The HMI imaging data captures the  $r, \theta, \phi$ -component of the solar magnetic field, and in our database, we keep the HMI  $B_r$  channel, which have demonstrated contains flare-predictive signals [24]. Finally, we derive the polarity inversion line (PIL) [22] from the  $B_r$ , which highlights a sub-region with the strongest flare discriminating signals [27, 23] and  $B_r \approx 0$ . In Figure 8, we plot one example of the 10 channels for an M-class flare.

For the particular case in Figure 8, the image size is  $377 \times 744$ , but different active regions are of different size. Also, different flares have their PIL, as well as the major signals in the other channels, stretching in different directions. To unify the size and orientation of all flares' imaging data, we follow these steps:

- Pick the pixel in the PIL channel with the largest sum of PIL weights near its  $51 \times 51$  neighborhood. This helps on picking the “center” of the image. If the PIL only contains zeros, which could happen for some very weak B-class flares, we use the AIA-1600Å instead.
- Around the “center” picked, we randomly sample 5,000 pixels, with replacement and the probability is proportional to the PIL mask value (or AIA-1600Å) pixel intensity, and do a Principal Component Analysis (PCA) of each pixel's 2D ( $x, y$ ) coordinates (coordinates on the pixel grid) and use the first principal component to calculate the orientation of the PIL. This technique helps to find the “direction” of the image.
- We rotate each channel with the same angle such that the “direction” of the PIL is vertical. Then, we crop a  $201 \times 201$  window around the “center” of the image, and do zero-padding where it is needed.

These preprocessing steps allow for the flare data to be roughly comparable, but just as the simulation data pattern in Figure 2, there is still randomness w.r.t. the positioning and direction of the flare predictive signal for each individual sample. We subset our flare list to those whose longitude is within  $\pm 60^\circ$  from the Sun's central meridian, which removes the low-quality samples with limb distortion. This reduces our sample size from 1,992 flares to 1,329 flares.

<sup>3</sup>See more details at <https://sdo.gsfc.nasa.gov/data/channels.php>

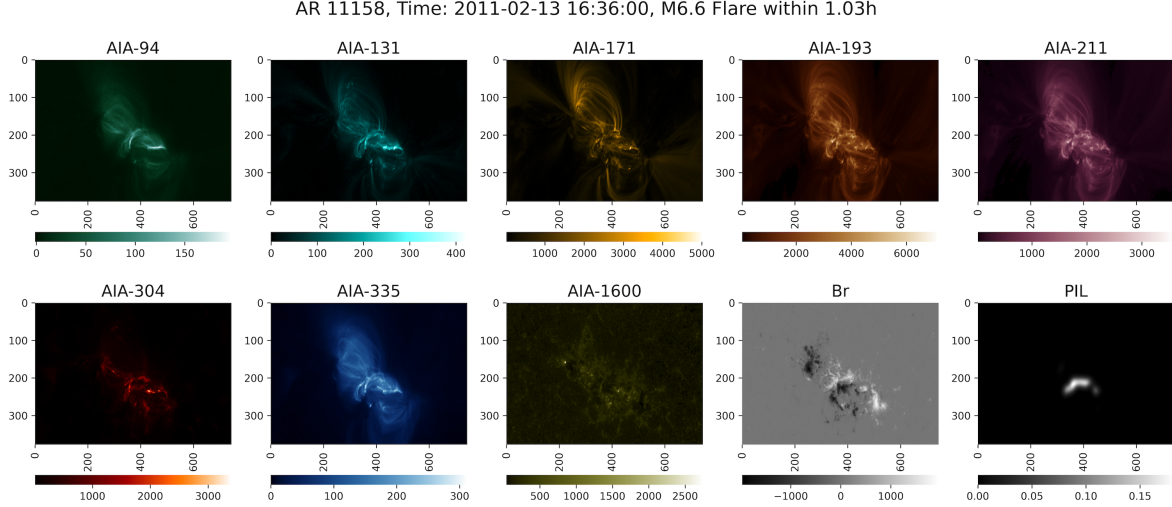


Figure 8: M-class Flare Example for Active Region (AR) No.11158, recorded at 16:36:00 (UT) of Feb 13, 2021. The flare intensity is  $6.6 \times 10^{-5} \text{W/m}^2$  and peaked at 17:38:00 (UT) of the same day. Tensor data size is  $377 \times 744 \times 10$ . Channel name labeled on top of each panel.

We further reduces the dimensionality of the  $201 \times 201$  images to  $50 \times 50$  by bi-linear interpolation to speed up the model computation. The pre-processed version of the sample in Figure 8, with tensor size  $50 \times 50 \times 10$ , is shown in Figure 9. Notice how the PIL channel is now looking more “vertical” and how each channel is sort of “zoomed-in”. The tensor size is now unified across all samples as  $50 \times 50 \times 10$ .

Before running the model, we normalize the scale of each channel such that each channel has its pixel intensity roughly within the range of  $[-1, 1]$ , to avoid numerical overflow in the algorithm. We only use the training set scale information to determine the scaling factor in order to avoid information spillover.

For the flare intensity, originally, B-class flare has its intensity within the interval  $[10^{-7}, 10^{-6}]$  (unit:  $\text{W/m}^2$ ), and M/X-class flare has its intensity within the interval  $[10^{-5}, 10^{-4}]$  (unit:  $\text{W/m}^2$ ). We transform any intensity  $y$  via:

$$\tilde{y} = \log_{10}(y) + 5.5$$

such that the middle point of the weakest M/X-class flare and the strongest B-class flare is centered at zero.

## F Additional Results on Solar Flare Forecasting

This appendix provides additional results on the solar flare intensity regression, we visualize the parameter estimates of **GPST-high** with random train/test split, which is the best-performing model in Table 2. Figure 10 provides the kernel estimates (the left three panels) and Figure 11 shows the non-zero feature maps.

The kernel estimators  $\hat{K}_1$  and  $\hat{K}_2$  indicate that feature map  $\mathcal{W}_{1,2}$  is of great importance since  $\hat{K}_1(1, 1)$  and  $\hat{K}_2(2, 2)$  contains the largest element, indicating that the feature extracted by  $\mathcal{W}_{1,2}$  explains the most variations across all feature maps.

In order to fully understand the covariance structure learnt with the multi-linear kernel estimators and the feature maps, one can decompose the variations of the regression label  $y$  given tensor data  $\mathcal{X} \in \mathbb{R}^{H \times W \times C}$  as follow:

$$\text{Var}(y) = \sum_{\substack{(s_1, t_1, c_1) \\ (s_2, t_2, c_2)}}^{h, w, C} \underbrace{K_1(s_1, s_2) \cdot K_2(t_1, t_2)}_{\text{Feature Map Importance}} \times \underbrace{\overbrace{K_3(c_1, c_2)}_{\text{Channel Importance}}}_{\text{Latent Features Product}} \times \underbrace{\left\langle \mathcal{W}_{s_1, t_1}, \mathcal{X}^{(c_1)} \right\rangle \cdot \left\langle \mathcal{W}_{s_2, t_2}, \mathcal{X}^{(c_2)} \right\rangle}_{\text{Latent Features Product}} + \overbrace{\sigma^2}^{\text{Noise}} \quad (44)$$

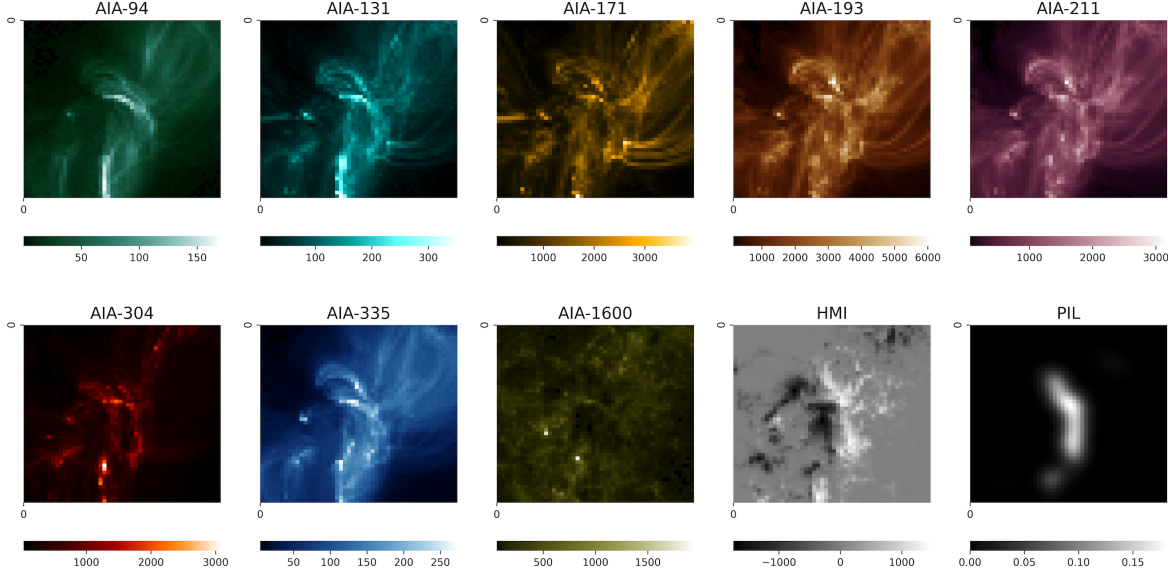


Figure 9: Pre-processed version of the sample in Figure 8. Notice how the PIL channel is now aligned vertically. Tensor size is reduced to  $50 \times 50 \times 10$  for all 1,329 flares.

and this leads to a natural definition of the percentage of explained variation for any single channel  $c^* \in \{1, 2, \dots, C\}$ :

$$\% \text{ Explained Variation} = \frac{K_3(c^*, c^*)}{\text{Var}(y)} \times \sum_{\substack{(s_1, t_1) \\ (s_2, t_2)}}^{h, w} \left\langle \mathcal{W}_{s_1, t_1}, \mathcal{X}^{(c^*)} \right\rangle \cdot \left\langle \mathcal{W}_{s_2, t_2}, \mathcal{X}^{(c^*)} \right\rangle \times K_1(s_1, s_2) \cdot K_2(t_1, t_2) \quad (45)$$

Any pair of distinct channels' percentage of explained variation can also be computed similarly. Similarly, one can define the percentage of explained variation for any feature map  $\mathcal{W}_{s^*, t^*}$  as:

$$\% \text{ Explained Variation} = \frac{K_1(s^*, s^*) \times K_2(t^*, t^*)}{\text{Var}(y)} \times \sum_{c_1, c_2}^{C, C} \left\langle \mathcal{W}_{s^*, t^*}, \mathcal{X}^{(c_1)} \right\rangle \cdot \left\langle \mathcal{W}_{s^*, t^*}, \mathcal{X}^{(c_2)} \right\rangle \times K_3(c_1, c_2) \quad (46)$$

The analysis here is a by-product of the Tensor-GPST model and is similar to the Joint and Individual Variation Explained (JIVE) [18] analysis and can be computed by estimating the latent features product using the training data. In the last two panels of Figure 10, we show the percentage of explained variation for all 10 AIA-HMI channels based on (45) and the percentage of explained variation for all 9 feature maps based on (46). Note that since all channels share the same set of feature maps, the latent features of different channel are not orthogonal, which indicates that the sum of the percentage of explained variation defined in (45) could exceed 100%. The same argument holds for the feature maps' explained variation.

The feature maps shown in Figure 11 mainly highlight two patterns:

- All six feature maps show non-zero weights on at least one of the four boundaries. This indicates that the features collected are around the perimeter of the flare eruptive region, which captures the “size” of the flare eruptive area. In Figure 12 and 13, we show the sample average of all 10 channels for the M/X-class and B-class flares, respectively. One can easily notice the difference between the two classes in terms of the “size” of the bright spots.
- There are some non-zero weights in  $\mathcal{W}_{1,2}$  and other feature maps near row 20, where features are collected near the top of the brightest PIL region of the M/X flares.

In Table 3, we include the results of different models on the solar flare intensity regression task with chronological train/test split. Compared to Table 2, we add one additional model, i.e. **GPST-medium** with  $\lambda = 0.5$ , that empirically shows less overfit and good fit on the training data.

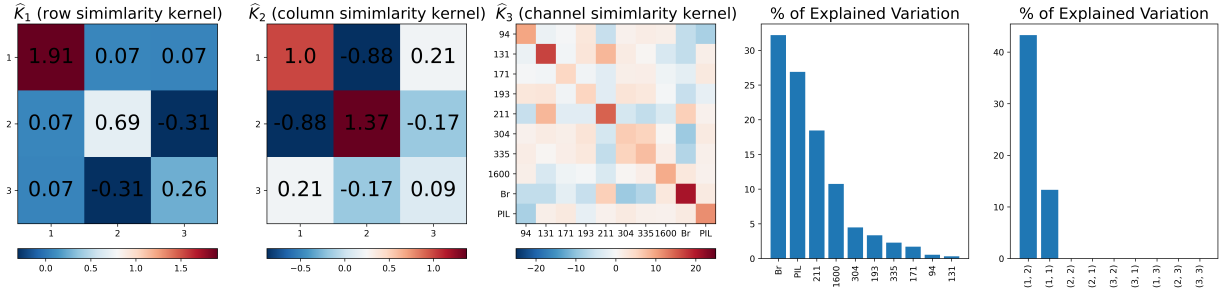


Figure 10: **GPST-high** (under random train/test split) kernel estimates (panel 1-3), channel-wise % of explained variations (panel 4) and feature map % of explained variations (panel 5). It coincides with the literature [27, 23] that the PIL is the channel with strong flare signals and the AIA imaging data is a good add-on to the HMI channel. The index for feature maps are the 2-tuple  $(s, t)$ .

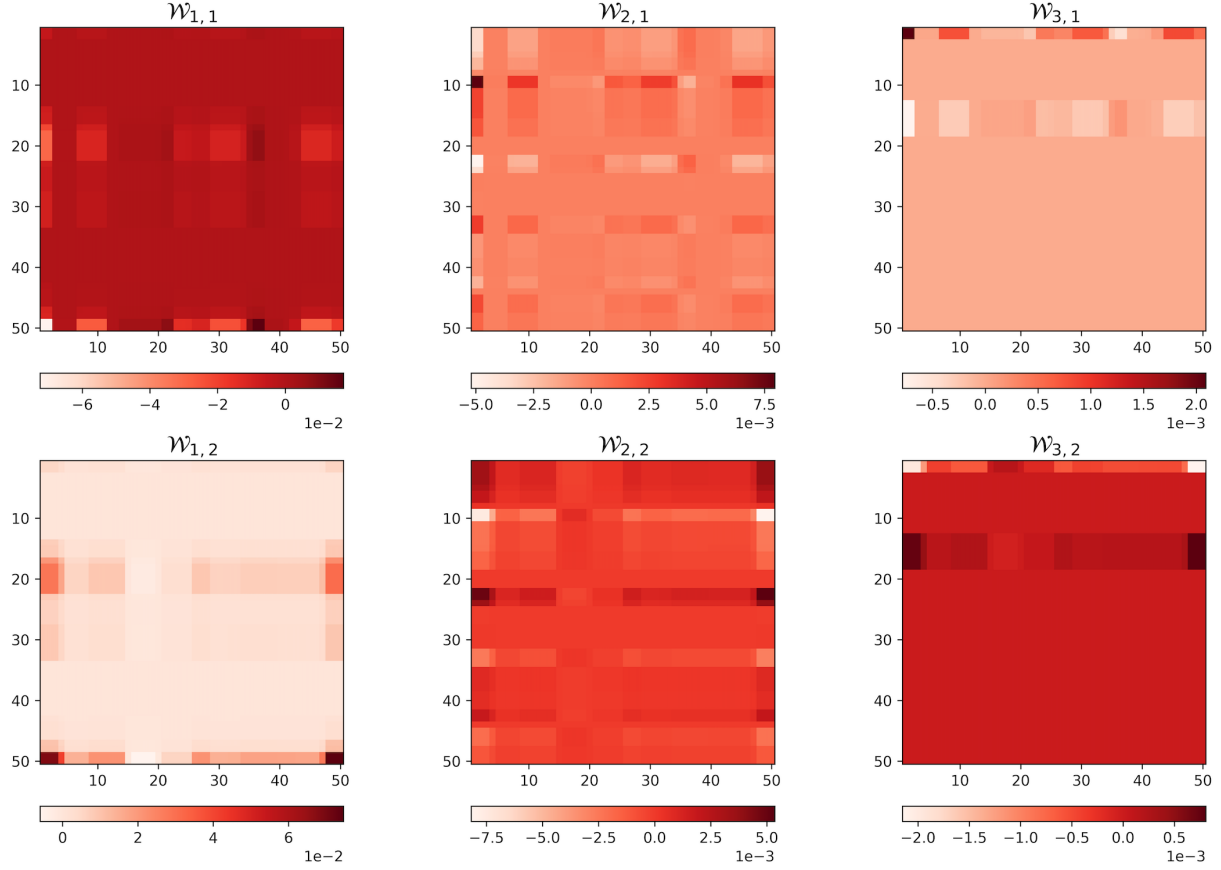


Figure 11: **GPST-high** feature map (the non-zero ones) estimates.

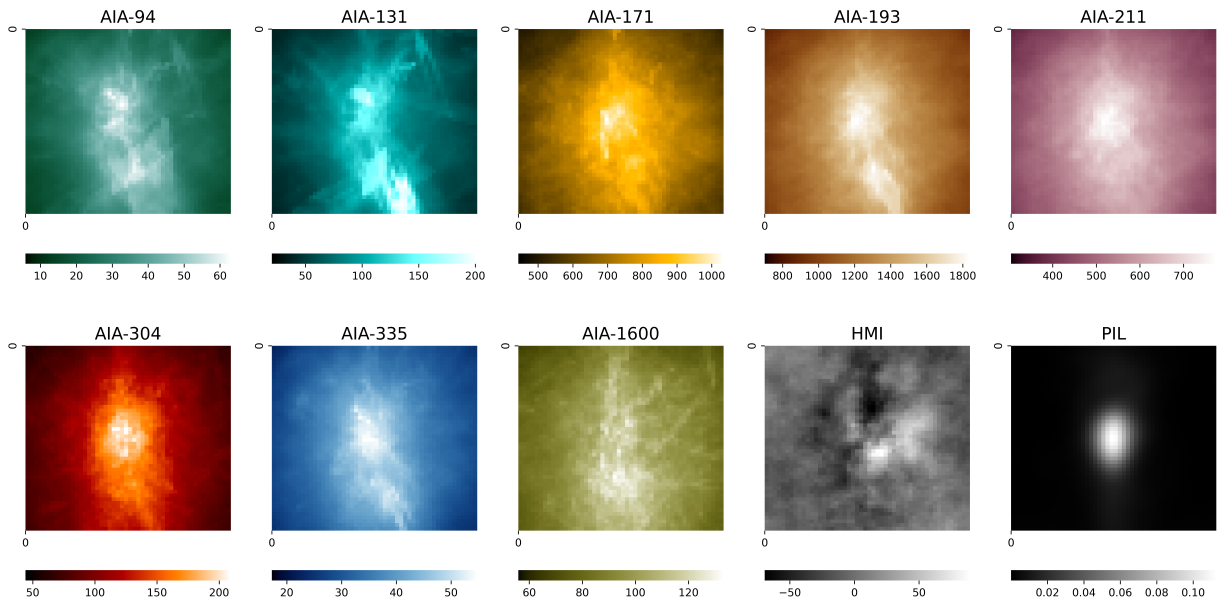


Figure 12: Sample average AIA-HMI map for M-class flare.

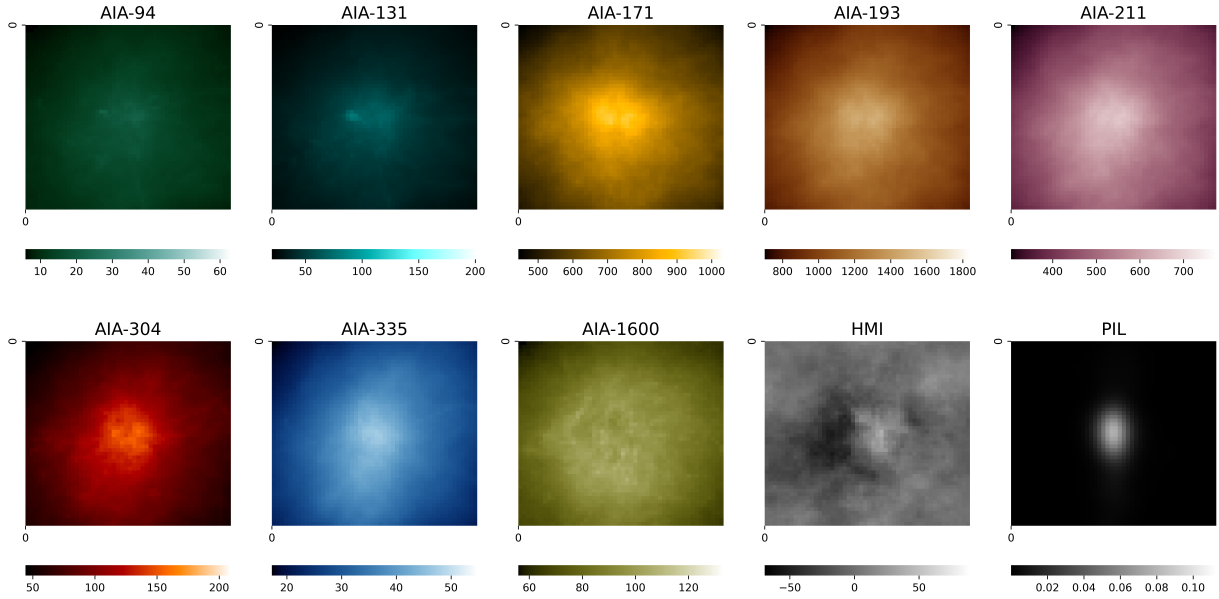


Figure 13: Sample average AIA-HMI map for B-class flare.

Model	MSE	R <sup>2</sup>	Pcover	TSS	$\hat{\sigma}$
<b>GP</b>	0.405 0.978	0.374 0.184	0.969 0.920	0.511 0.309	0.662
<b>GPST-low</b>	<b>0.392</b> 0.772	<b>0.394</b> 0.220	0.968 0.900	<b>0.518</b> 0.366	0.634
<b>GPST-medium</b>	0.429 <b>0.611</b>	0.337 0.269	<b>0.970</b> <b>0.957</b>	0.448 <b>0.432</b>	0.661
<b>GPST-high</b>	0.414 0.720	0.361 0.235	0.960 0.925	0.476 0.338	0.649
<b>CP</b>	0.452 0.648	0.303 <b>0.310</b>	—	0.438 0.400	—
<b>Tucker</b>	0.462 0.655	0.287 0.301	—	0.428 0.400	—

Table 3: Solar Flare intensity regression results on training (top) and testing (bottom) set across six different models under chronological train/test splitting. The metrics are mean-squared-error (MSE), R-squared, Coverage Probability (Pcover), True Skill Statistics (TSS) and the estimated noise standard deviation  $\hat{\sigma}$ . Best training/testing set results are highlighted in boldface.